



ACT Project Number:
271498

Project name:
ELEGANCY

Project full title:
Enabling a Low-Carbon Economy via Hydrogen and CCS

ERA-Net ACT project

Starting date: 2017-08-31
Duration: 36 months

D1.1.2
Report on characterization of equilibria and transport phenomena in promising new adsorbents for CO₂/H₂ separation

Date: 2019-08-30

Organization name of lead participant for this deliverable:
ETH Zurich

ACT ELEGANCY, Project No 271498, has received funding from DETEC (CH), BMWi (DE), RVO (NL), Gassnova (NO), BEIS (UK), Gassco, Equinor and Total, and is cofunded by the European Commission under the Horizon 2020 programme, ACT Grant Agreement No 691712.		
Dissemination Level		
PU	Public	X
CO	Confidential, only for members of the consortium (including the Commission Services)	

Deliverable number:	D1.1.2
Deliverable title:	Report on characterization of equilibria and transport phenomena in promising new adsorbents for CO ₂ /H ₂ separation
Work package:	WP1 – H ₂ supply chain and H ₂ -CO ₂ separation
Lead participant:	ETHZ

Authors		
Name	Organisation	E-mail
Anne Streb*	ETHZ	streb@ipe.mavt.ethz.ch
Mijndert van der Spek	ETHZ	m.van_der_spek@hw.ac.uk
Jens Jørsboe	ETHZ	jensj@student.ethz.ch
Mehrdad Asgari	EPFL	mehrdad.asgari@epfl.ch
Wendy Queen	EPFL	wendy.queen@epfl.ch
Marco Mazzotti	ETHZ	marco.mazzotti@ipe.mavt.ethz.ch

*lead author

Keywords
Zeolite 13X, Activated Carbon, MOF, Cu-TDPAT, zeolite CaX, mixed-matrix adsorbents, adsorption isotherm, breakthrough experiments, H ₂ , CO ₂ , N ₂ , CH ₄ , CO, Ar, mass transfer, heat transfer

Abstract
<p>Vacuum pressure swing adsorption (VPSA) for CO₂-H₂-impurity separation can be a key technology for coupling fossil fuel based H₂ production with carbon capture and storage (CCS), thereby enabling the fossil-fuel based production of H₂ with low associated CO₂ emissions at a large scale and competitive cost in a timely manner.</p> <p>For such a VPSA process to operate at its optimum, it is crucial to choose the right adsorbent(s). The adsorbent requirements are different for a process targeting co-production of high purity H₂ and CO₂ from a multicomponent feed at high recoveries for both products, compared to a process which targets the purification of either one or the other. These include a high CO₂ cyclic capacity, an intermediate adsorption of the impurities and little H₂ adsorption. In addition, a low heat of adsorption and fast mass transfer kinetics are favorable.</p> <p>This report starts with a sensitivity analysis to assess the influence of different adsorbent-related parameters on the process performance. Whereas the heat of adsorption and the mass transfer of CO₂ play an important role, they are less important for the impurities (CO, CH₄, N₂) and the separation performance is barely influenced by the heat of adsorption or mass transfer of H₂. An accurate description of the isotherms</p>

including their temperature dependence is important not only for CO₂, but also for the impurities. For H₂, however, not knowing the temperature dependence of the isotherm or neglecting H₂ adsorption all together influences the separation performance only a little.

Commercial adsorbents have large potential both for H₂ purification and for CO₂ capture applications, especially when fast increase in technology readiness level (TRL) is necessary, as is the case here. Commonly used adsorbents include zeolites and activated carbons.

Three commercial adsorbents, namely zeolite 13X, zeolite CaX and activated carbon AP3-60, were characterized by measuring the adsorption isotherms for CO₂, several impurities like CH₄, N₂, CO and Ar relevant in H₂ production processes, and H₂ (not on zeolite CaX). The isotherms were fitted with a temperature dependent Sips adsorption isotherm equation for all components. The heat of adsorption was determined from the temperature dependent adsorption isotherms and is very high for CO₂ on zeolite CaX, which is unfavorable for the separation.

Zeolite 13X performs particularly well for VPSA and therefore was further characterized by performing binary and ternary breakthrough experiments with CO₂-H₂-CH₄ mixtures. Both mass and heat transfer parameters were estimated using a 1D adsorption column model. The model can reproduce the experimental results very well for binary breakthrough experiments, but the agreement is worse for the prediction of ternary breakthrough experiments. Constant mass transfer coefficients can be assumed, whereas the heat transfer has to be estimated individually for each experiment.

In addition to commercial adsorbents, also novel adsorbents show promise for CO₂ capture and H₂ purification. A Cu-TDPAT metal organic framework (MOF) was characterized by measuring CO₂, H₂, CO, CH₄ and N₂ isotherms, fitting isotherm parameters and computing the heats of adsorption. Whereas the heat of adsorption is low for CO₂ and the uptake and cyclic capacity very high, the low N₂ adsorption makes it difficult to produce high purity H₂ with Cu-TDPAT. This issue could be resolved by mixing Cu-TDPAT and zeolite CaX, which features a high N₂ adsorption. Isotherms on three discrete mixtures were determined showing that the N₂ adsorption can be enhanced when adding zeolite CaX to Cu-TDPAT, whereas the CO₂ adsorption decreases.

Overall, this report provides valuable data for modelling VPSA processes with different adsorbents and gives an insight into process implications and limitations when choosing one or the other material.

TABLE OF CONTENTS

	Page
1 INTRODUCTION.....	2
2 METHODOLOGY	4
2.1 Measurement of adsorption isotherms	4
2.2 Breakthrough Experiments	7
3 SENSITIVITY ANALYSIS.....	12
3.1 Methodology	12
3.2 Base case cycle performance	13
3.3 Sensitivity analysis on mass transfer coefficient	14
3.4 Sensitivity analysis on heat of adsorption.....	15
3.5 Sensitivity analysis on adsorption isotherms.....	17
3.6 Summary of sensitivity analysis.....	21
4 COMMERCIAL ADSORBENTS	22
4.1 Zeolite 13X	22
4.2 Breakthrough experiments	24
4.3 Zeolite CaX.....	33
4.4 Activated Carbon	37
5 NOVEL ADSORBENTS	40
5.1 Cu-TDPAT	40
6 COMPARISON OF DIFFERENT ADSORBENTS.....	44
6.1 CO ₂ adsorption and cyclic capacity	44
6.2 The role of impurity adsorption	46
7 MIXED-MATRIX ADSORBENTS	50
7.1 Adsorption isotherms.....	50
7.2 Isotheric heat of adsorption	53
8 SUMMARY AND CONSLUSION.....	55
BIBLIOGRAPHY.....	58

1 INTRODUCTION

Hydrogen with low associated CO₂ emissions is expected to play an important role in future energy systems with uses in the decarbonisation of industry, transportation and heating. Whereas in the long term, the production of carbon neutral hydrogen through electrolysis using renewable energy is likely to be the preferred option, in the short term this production route is unlikely to provide hydrogen at required scale and competitive cost.

An alternative, with the potential to produce large amounts of hydrogen with low associated carbon emissions in a timely manner, is the coupling of fossil fuel based hydrogen production with carbon capture and storage (CCS). Elegancy examines this option.

Already today, fossil fuel based H₂ production is performed at large scale for uses in refineries and ammonia or methanol production. Main technologies include steam methane reforming (SMR) and autothermal reforming (ATR) of natural gas. For both processes, a pressure swing adsorption (PSA) unit follows the reformer and one or two water-gas shift (WGS) reactors to purify hydrogen up to the purities required for the applications of interest. Typical hydrogen purity requirements e.g. for catalytic boilers, refineries or stationary fuel cells are 99.9 %. For fuel cells for transportation, even higher purities of 99.97 % are required [1].

Different options for separating CO₂ from a gaseous process stream at various concentrations exist. The most mature technology for CO₂ capture is wet scrubbing using physical or chemical solvents. In the context of H₂ production, there are several possibilities for separating CO₂ from the process. The IEAGHG identified a capture step after the WGS and before the PSA as most economical [2]. However, all the options they examined require a new separation stage as addition to the existing H₂ production process. A promising alternative is the combination of H₂ purification and CO₂ separation within a single adsorption unit. Vacuum pressure swing adsorption (VPSA) cycles for the purpose of this co-production of CO₂ and H₂ within a single cycle have been developed and are reported in D1.1.1 [3] and in a recent paper [4]. Typical inlet streams to the VPSA unit contain hydrogen (produced as the light product from the VPSA unit due to little adsorption), CO₂ (produced as the heavy product, strongly adsorbed) and impurities including CH₄, N₂, Ar (for ATR only) and CO.

It is important to stress that the performance of every adsorption process is strongly dependent on the adsorbent used. A process can only perform at its optimum when choosing an appropriate adsorbent. In contrast to processes that require only the purification of either the light (here: H₂) or the heavy (here: CO₂) product, the requirements for an adsorbent for such a dual separation where both light and heavy product have to be purified are different [3]. The adsorbent should feature a:

- high cyclic capacity for CO₂ for the operating conditions (here: between above ambient or ambient pressure to a vacuum in the range of 0.1 to 0.2 bar)
- high selectivity of CO₂ over H₂ and all impurities, to be able to separate CO₂ at high purity
- high selectivity of CO₂ and all impurities over H₂ to be able to purify H₂ during the adsorption step

- a low heat of adsorption and fast kinetics are favorable for the separation

This report first explains the methodology for the conducted experiments including isotherm measurements and breakthrough experiments and the fitting of mass and heat transfer parameters from those breakthrough experiments.

Second, with the help of a sensitivity analysis, the report highlights which data is essential for process modelling and optimization.

Third, measured isotherm data is shown and discussed for different relevant components on three commercial adsorbents (zeolite 13X, zeolite CaX and activated carbon AC), a novel metal organic framework (MOF) named Cu-TDPAT, and mixed matrix adsorbents consisting of different mixtures of Cu-TDPAT and zeolite CaX. Suitable isotherm equations are used to fit the measured data. The heat of adsorption is provided for all materials. This part includes a comparison between the different adsorbents together with a discussion of more and less favorable characteristics. For zeolite 13X, breakthrough experiments will be shown and the fitted mass transfer and heat transfer parameters will be discussed.

2 METHODOLOGY

2.1 Measurement of adsorption isotherms

Different possibilities exist for measuring adsorption isotherms. In this work, two different methods were used for measuring single component isotherms, namely gravimetric and volumetric method.

For the gravimetric method, a Rubotherm magnetic suspension balance (MSB) was used. A dual sinker configuration allows for the simultaneous measurement of the mass change of the sample during adsorption and the bulk density. Both setup and evaluation of the measurements have been explained in detail elsewhere [5, 6, 7]. Therefore only the main characteristics are summarized. The measurements were carried out mainly in desorption mode, but some measurements were repeated in adsorption mode to ensure that there is no hysteresis and test the reproducibility. The procedure was as follows:

1. Regeneration of the sample (combination of vacuum and heat)
2. Volume measurement using He (non-adsorbed) at high pressure (50-200 bar) and temperature (150-200 °C)
3. Evacuation and heating to target isotherm temperature
4. Measurement of zero value
5. Isotherm measurement

The regeneration method (step 1) depends on the adsorbent used and is summarized in Table 1. Steps 1 and 5 were repeated for all different isotherms (different temperatures and components). For hydrogen adsorption on zeolite 13X, the density of H₂ and the low adsorption made the measurements difficult. In order to obtain reproducible results, the zero value was measured after every single point (step 4) by evacuation the balance.

The excess amount adsorbed, which is the true measurable quantity, was converted to the absolute amount adsorbed assuming the adsorbed phase density to be equal to the liquid density at specific conditions. These are the boiling point for H₂, CH₄ and Ar and 18 MPa and 0 °C for CO₂ [5].

For the volumetric method, a Belsorp-max was used for all isotherms up to one bar. For high-pressure volumetric data, a Micromeritics HPVA was used. The density cannot be measured directly, but was calculated using an equation of state. The procedure has been explained by Asgari et al. [8].

2.1.1 Isotherm equations

Many different forms for the mathematical description of single component isotherms exist. Explicit isotherm equations are particularly useful for modelling adsorption processes. We adapt two widely used explicit isotherm models for fitting the isotherm data, namely the Sips isotherm and the dual site Langmuir isotherm. The dual site Langmuir isotherm is an extension of the standard Langmuir isotherm assuming two energetically different sites, both characterized by their saturation capacity a_i^{inf} and c_i^{inf} and their equilibrium constant b_i and d_i . In this work, we describe the single temperature isotherm data on Cu-TDPAT, zeolite CaX and mixtures of Cu-TDPAT and zeolite CaX with a DSL isotherm.

$$q_i = \frac{a_i^{\text{inf}} b_i P}{1 + b_i P} + \frac{c_i^{\text{inf}} d_i P}{1 + d_i P}$$

The Sips isotherm extends the standard Langmuir isotherm by an exponent s_i .

$$q_i = \frac{a_i^{\text{inf}} (b_i P)^{s_i}}{1 + (b_i P)^{s_i}}$$

The temperature dependence of the Sips isotherm is given as follows for Cu-TDPAT and zeolite CaX (and for zeolite 13X as used in the sensitivity analysis):

$$a_i^{\text{inf}}(T) = A_{1,i} + A_{2,i} T$$

$$b_i(T) = B_{0,i} \exp\left(\frac{B_{1,i}}{T}\right)$$

$$s_i(T) = \frac{1}{C_{1,i} + \frac{C_{2,i}}{T}}$$

as follows for zeolite 13X:

$$a_i^{\text{inf}}(T) = a_{1,i} \exp\left(a_{2,i} \left(\frac{T}{T_{\text{ref}}} - 1\right)\right)$$

$$b_i(T) = b_{0,i} \exp\left(\frac{b_{1,i}}{RT}\right)$$

$$s_i(T) = c_{1,i} + c_{2,i} \left(\frac{T}{T_{\text{ref}}} - 1\right)$$

and as follows for activated carbon:

$$a_i^{\text{inf}}(T) = \alpha_{1,i} \exp\left(-\frac{\alpha_{2,i}}{RT}\right)$$

$$b_i(T) = \beta_{0,i} \exp\left(-\frac{\beta_{1,i}}{RT}\right)$$

$$s_i(T) = \gamma_{1,i} \text{atan}(\gamma_{2,i}(T - T_{\text{ref}})) + \gamma_{3,i}$$

with the reference temperature T_{ref} and the fitting parameters $A_{1,i}$ - $C_{2,i}$, $a_{1,i}$ - $c_{2,i}$, and $\alpha_{1,i}$ - $\gamma_{2,i}$.

2.1.2 Isosteric Heat of adsorption

The isosteric heat of adsorption ΔH_i^{iso} is an important parameter and can be determined from isotherm measurements at different temperatures using the Clausius Clapeyron equation. This equation relates the change in pressure to the change in temperature at a constant adsorbed amount q_i :

$$\Delta H_i^{\text{iso}}(q_i, T) = -R \left. \frac{\partial \ln(P)}{\partial \left(\frac{1}{T}\right)} \right|_{q_i}$$

The isosteric heat is temperature and loading dependent. In process modelling, often an isosteric heat averaged over different temperatures is applied. To obtain a temperature averaged isosteric heat, constructed experimental data at the same loading was used, as described in detail by Schell et al. [5]. For this constructed data, $\ln(P)$ was plotted over $1/T$ and fitted with straight lines. The temperature averaged isosteric heat of adsorption was determined from the slope of this fit. For the evaluation, only loadings up to which data at three different temperatures was available were considered.

In case not only a temperature averaged, but also a loading independent isosteric heat is needed, which is often the case in process modelling, this can be computed from the loading dependent isosteric heat averaged over the loading range of interest.

2.1.3 Experimental campaign

The different adsorbents that were used in this work are summarized in Table 1 below together with the regeneration method applicable for the different setups. Three different mixtures of Cu-TDPAT and zeolite CaX were examined with 40, 60 and 80 w% Cu-TDPAT. The addition of CaX was expected to enhance the low N_2 adsorption of Cu-TDPAT. This will be explained in more detail in later sections. The isotherm measurements are summarized in Table 2. For zeolite 13X, also the regeneration for the breakthrough experiments (section 2.2) is included in Table 1.

Table 1 – Different adsorbents used for measuring single component isotherms. The regeneration method is different for each adsorbent and can depend on the setup used. For Cu-TDPAT and zeolite CaX, the same regeneration temperature was chosen, because this enables a mixing of zeolite CaX with Cu-TDPAT to enhance the low nitrogen adsorption of the MOF.

Adsorbent	form	supplier	setup	regeneration
Zeolite 13X	pelletized	Zeochem	gravimetric	> 4 h vacuum, 400 °C
Zeolite 13X	pelletized	Zeochem	breakthrough	> 2 h vacuum, 250 °C
Activated carbon AP3-60	pelletized	Chemviron Carbon	gravimetric	> 4 h vacuum, 150 °C
CaX	powder	synthesized ¹	gravimetric/ volumetric	12 h vacuum, 220 °C
Cu-TDPAT	powder	synthesized ²	gravimetric	> 5 d evacuation, then 12 h vacuum, 220 °C
Cu-TDPAT	powder	synthesized ¹	volumetric	12 h vacuum, 220 °C
Cu-TDPAT-CaX-mix	powder	synthesized ^{1,2}	volumetric	12 h vacuum, 220 °C

¹Synthesized by our collaborators at EPFL, ion exchange according to Sherry [9]

²Synthesized by our collaborators at EPFL according to Li et al. [10]

Table 2 – Experimental campaign with all isotherm measurements including the different adsorbents, the method used and the different gases, temperatures and pressures.

Adsorbent	Gas	Setup	Temperature [°C]	Pressure [bar]
Zeolite 13X	H ₂ , CH ₄ , Ar	gravimetric	25, 45, 65	0-30
AC	Ar, CH ₄	gravimetric	25, 45, 65	0-30
Zeolite CaX	CO ₂	gravimetric	25, 65	0-30
Zeolite CaX	CO ₂ , CO, CH ₄ , N ₂	volumetric	15, 25, 35	0-1
Cu-TDPAT	CO ₂ , CO, CH ₄ , N ₂	volumetric	15, 25, 35	0-1
Cu-TDPAT	CO ₂	gravimetric	25	0-30
Cu-TDPAT	CO ₂	volumetric	25	0-30
Cu-TDPAT	H ₂	volumetric	25	0-200
Cu-TDPAT- CaX mix	CO ₂ , CO, CH ₄ , N ₂	volumetric	15, 25, 35	0-1

2.2 Breakthrough Experiments

2.2.1 Experimental

Breakthrough experiments were carried out for estimating mass and heat transfer parameters for different components, for validating model accuracy by comparing the experiments with the modelling results and for testing the model's predictive capability. The breakthrough experiments were carried out in the laboratory setup described in detail in M1.1.2 [11]. The setup is shown without the storage section in Figure 1. The core of the experimental setup are two double-jacketed columns that allow for an active heating and cooling of both columns. The inflow can be controlled using four different mass flow controllers (MFC) and the outflow can be monitored using three mass flow meters (MFM) in series in combination with a mass spectrometer (MS) to analyze the composition of the gas phase. Two different mixtures were used for the breakthrough experiments. They are reported in

Table 3 indicated as mixtures 1 and 2. Mixture 3 was used for calibrating the MS only. All gases were obtained from Pangas, Switzerland with a tolerance of ± 1 % (rel.).

The MS was calibrated prior to every set of two experiments using the feed mixture for binary breakthrough experiments and the feed mixture together with mixture 1 and mixture 3 for ternary breakthrough experiments.

Before all experiments, both columns were packed with zeolite 13X with a particle size of 1.6 to 2.0 mm as used in previous works [12]. Before each experiment, the corresponding column is regenerated by heating to 250 °C and applying a vacuum for a minimum of 2

hours. After a maximum of three experiments, a more thorough regeneration was performed by heating to 250 °C overnight for at least 12 hours. No difference was found for experiments performed with these different regeneration procedures. After the regeneration, the column was filled with Helium to the adsorption pressure. Subsequently, the inlet was switched to the feed mixture. The temperatures and pressures within the column, the outflow velocity and the composition after the column were monitored continuously.

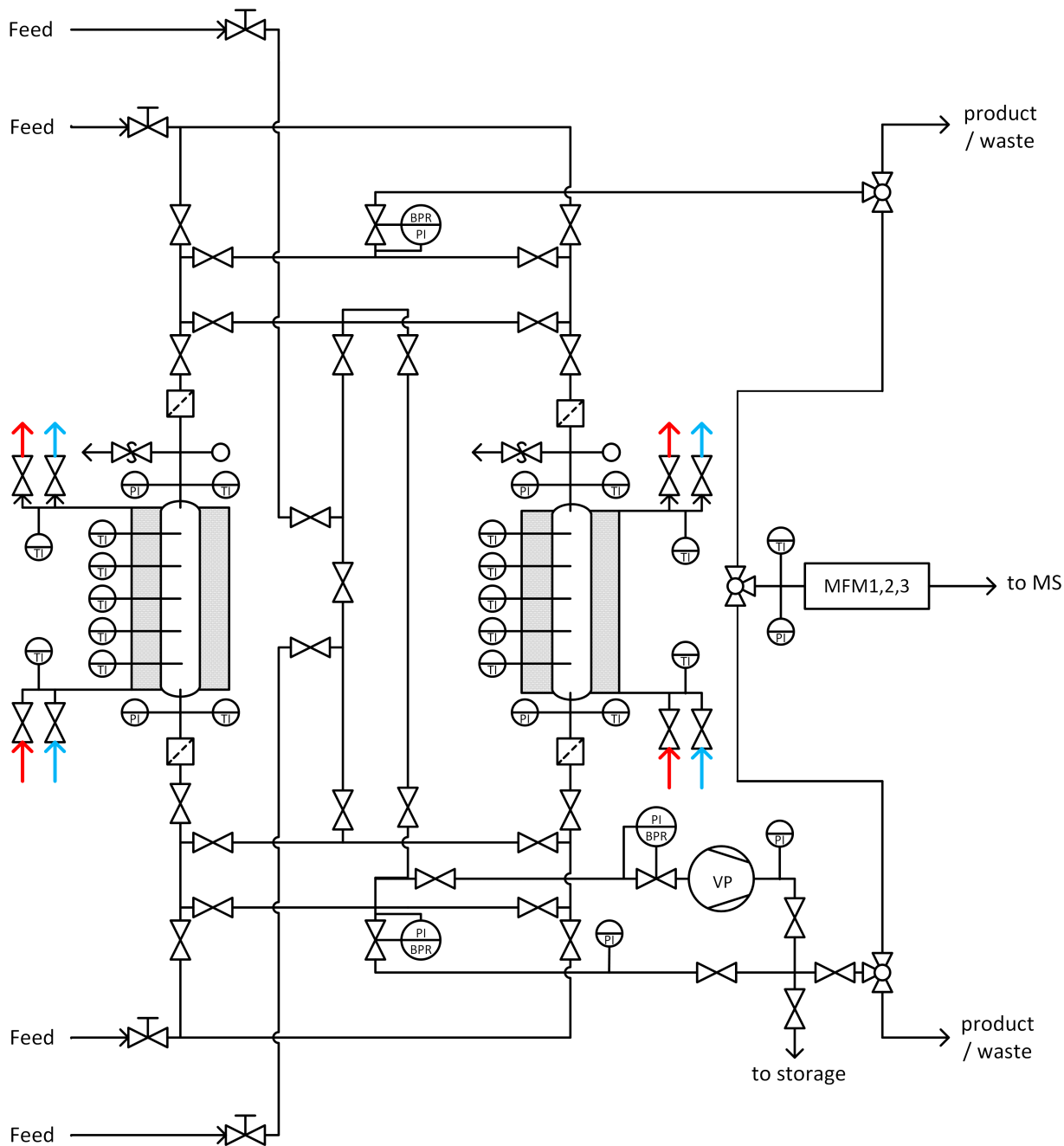


Figure 1 – VPSA lab setup used for breakthrough experiments. The upstream equipment (MFCs, valves, piping, gas bottles), the storage section and the downstream composition analysis (MS) are not shown.

Table 3 – Gas mixtures used for breakthrough experiments on zeolite 13X (mixtures 1 and 2) and for calibrating the MS (mixtures 1-3).

	CO ₂	CH ₄	H ₂	unit
Mixture 1	50	50	0	mol%
Mixture 2	20	5	75	mol%
Mixture 3	0	50	50	mol%

2.2.2 Modelling

For fitting the transport parameters, the column temperatures and the composition of the outflow were compared to modelling results by minimizing the following objective function:

$$\Phi_{obj} = 0.5 \sum_{k=1}^2 \ln \left(\frac{1}{N_{obs,y}} \sum_{j=1}^{N_{obs,y}} \left(\frac{y_{j,k} - \hat{y}_{j,k}(p)}{y_{j,k} + 1} \right)^2 \right) + 0.5 \sum_{k=1}^5 \ln \left(\frac{1}{N_{obs,y}} \sum_{j=1}^{N_{obs,y}} \left(\frac{T_{j,k} - \hat{T}_{j,k}(p)}{T_{j,k}} \right)^2 \right)$$

with the modelled temperatures $T_{j,k}$ and mole fractions $y_{j,k}$ at time j and the experimental values $\hat{y}_{j,k}$ and $\hat{T}_{j,k}$. The procedure has been explained in detail by Marx et al. [12].

The parameters of interest are mass transfer parameters for CO₂, H₂ and CH₄ and heat transfer parameters for the heat transfer inside the column to the wall. Furthermore, the feed velocity is included as fitting variable to compensate for the intrinsic errors of the MFC.

The model used has been explained in detail elsewhere, therefore only the main characteristics and peculiarities necessary to describe breakthrough experiments are repeated. The model is 1D and makes use of a mass and energy balance coupled with the Ergun equation to account for the pressure drop inside the column. Mass transfer is described with a linear driving force approximation with the linear driving force coefficient k_i :

$$\frac{\partial q_i}{\partial t} = k_i(q_i^* - q_i)$$

Where q_i and q_i^* are the actual and equilibrium adsorbed phase concentration of species i . For modelling multicomponent adsorption throughout the fitting of the breakthrough experiments, we make use of the ideal adsorbed solution theory (IAST) rather than of extended isotherms. Extended single component isotherms are often used in process modelling because they give an explicit formulation for the adsorbed amount. IAST requires an iterative solution and is therefore computationally more intensive. IAST is a framework that describes mixed-gas adsorption when the adsorbed phase behaves ideally and was implemented as explained by Schell et al. [5].

The heat transfer was accounted for as explained by Marx et al. [12] with one heat transfer coefficient h_c that lumps the heat transfer inside the column and to the column wall. This coefficient was fitted individually to each experiment. A second heat transfer coefficient h_w was used to describe the heat transfer through the column wall to the thermofluid. This external heat transfer coefficient depends on thermostat and thermofluid properties, on the column geometry and on the temperature. An average value of $h_w = 220 \text{ W}/(\text{m}^2\text{K})$ is used. The details of the determination of the heat transfer coefficient have been explained by Marx et al. [12].

Because of the piping upstream and downstream of each column, there is a delay between the outlet of each MFC and the inlet of a column as well as between the outlet of the column and the inlet of the MS. The upstream piping can be accounted for with a simple time shift. For the downstream piping, this is not possible because composition and flowrate vary. Therefore, they were included in the modelling, as described in detail by Casas et al. [13]. Diffusion was neglected in the whole setup. The important parameters for the fitting of the breakthrough experiments are summarized in Table 4.

Table 4 – Parameters for the laboratory VPTSA setup and for modelling the breakthrough experiments.

parameter	symbol	unit	value
Column length	L	[m]	1.2
Internal radius	R_i	[m]	12.5×10^{-3}
External radius	R_o	[m]	15×10^{-3}
Heat capacity wall	C_w	[J/(m ³ K)]	4×10^6
External heat transfer coefficient	h_w	[W/(m ² K)]	220
Zeolite 13X material density	ρ_m	[kg/m ³]	2359
Particle density	ρ_p	[kg/m ³]	1085
Bed density	ρ_b	[kg/m ³]	507
Particle diameter	d_p	[m]	1.8×10^{-3}
Heat capacity sorbent	C_s	[J/(kg K)]	1100 ¹
Isosteric heat of adsorption	ΔH_i^{iso}	[J/mol]	CO ₂ : 37000; CH ₄ : 22300; H ₂ :11000; see Figure 8
Isotherm parameters	See Table 9		

¹An average based on literature values was chosen [14] [15]

2.2.3 Experimental campaign

The focus of the experimental campaign was to determine the mass and heat transfer parameters on zeolite 13X for mixtures of CO₂, CH₄ and H₂. The mass transfer of N₂ had already been characterized in previous experiments by Marx et al. [12]. In these experiments, it was shown that the heat transfer is more important than the mass transfer for successfully describing breakthrough experiments when using a material with a high heat of adsorption, as e.g. zeolite 13X or also Cu-TDPAT. Therefore, we limited our study to the best material we found so far for the co-purification of CO₂ and H₂ – zeolite 13X – , the two products – CO₂ and H₂ – and the major impurity – CH₄. No breakthrough experiments were carried out on AC, because we have found that this material is not very promising for the separation of interest [3].

Moreover, no breakthrough experiments on Cu-TDPAT or CaX were carried out. First, because it can be assumed that they are similarly insensitive to the mass transfer coefficient, as they feature a higher heat of adsorption for CO₂ than zeolite 13X. Second, the amounts synthesized were small and insufficient to carry out these experiments. Finally, these materials were available as powder and not pelletized, potentially leading to results that are not representative for the pelletized material.

The following set of eight breakthrough experiments was carried out on zeolite 13X:

Table 5 – Experimental campaign for breakthrough experiments on zeolite 13X.

	flowrate	pressure	temperature
	[cm ³ /s]	[bar]	[°C]
CO ₂ :CH ₄ 50:50	20	1, 10, 25	25
CO ₂ :CH ₄ 50:50	20	10, 25	45
CO ₂ :CH ₄ :H ₂ 20:5:75	20	10, 25	25
CO ₂ :CH ₄ :H ₂ 20:5:75	40	10	25

3 SENSITIVITY ANALYSIS

3.1 Methodology

A sensitivity analysis was carried out to assess the influence of mass transfer, heat of adsorption and isotherms on the performance of a given cycle. The mass transfer coefficients (assuming a linear driving force model), the heat of adsorption, the temperature invariant maximum capacity at infinite pressure and the temperature dependence of the isotherm were varied whilst keeping the cycle and all other process parameters including the step durations, the recycle ratio, the evacuation pressure and the flowrates constant.

The column model is the same as described in section 2.2.2 without any upstream or downstream piping. The cycle used for the sensitivity analysis has been described in D1.1.1 [3] and is shown in Figure 2 below. As basis for the sensitivity analysis, an operating point that can fulfill strict purity and recovery requirements for both CO₂ and H₂ with > 90 % recovery for both, > 99.97 % H₂ purity and > 96 % CO₂ purity was chosen.

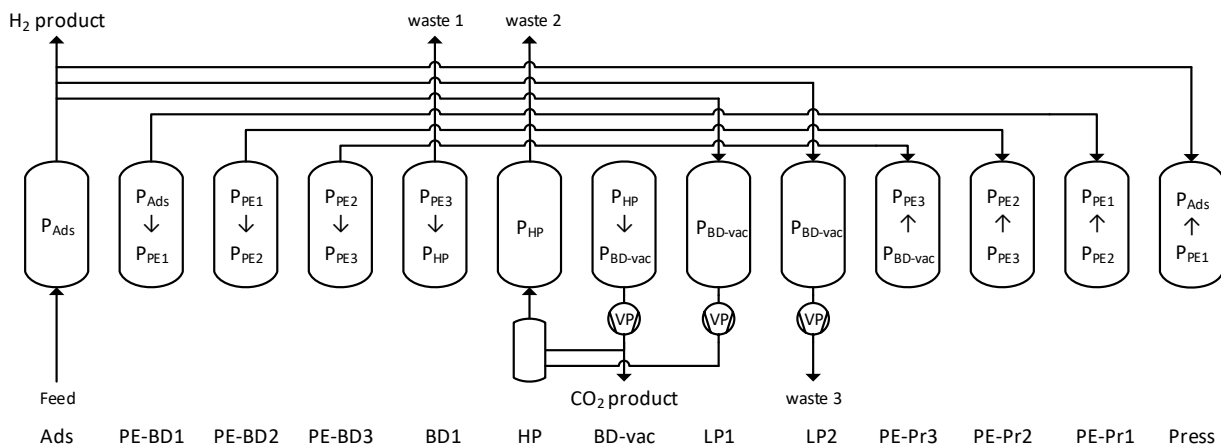


Figure 2 – VPSA cycle for co-production of CO₂ and H₂.

Isotherms, average heats of adsorption and mass transfer coefficients are taken from literature [16] and are the same as used in D1.1.1 [3]. Extended Sips isotherms were used for modelling multicomponent adsorption. The temperature dependence of the isotherms was described in the same way as for Cu-TDPAT and zeolite CaX. The relevant isotherm parameters are reported in Table 6.

The upper and lower boundaries for the sensitivity analysis on the heat of adsorption were based on the upper and lower boundaries for the loading dependent but temperature averaged heats of adsorption as reported by Park et al. [16]. They are reported in Table 6 together with the other isotherm parameters. For the mass transfer coefficient k_i , half and double the values from the base case are taken as lower and upper bound. These values were found to cover the range measured in our group for CO₂ and N₂ on the same material [12] as well as the values reported in the literature [16]. For the sensitivity analysis on the isotherms, the temperature invariant maximum capacity $A_{1,i}$ was varied by $\pm 10\%$ to set the upper and lower bound. In addition, a case without temperature dependence was assessed by calculating the value for a_i^{inf} , b_i and s_i at 35 °C and by setting the temperature dependence of the isotherm to zero.

The sensitivity analysis was performed by setting one value at a time to the lower or upper bound. In addition, the effect of setting all of them simultaneously to the high or low value was assessed for the mass transfer coefficient, the heat of adsorption, the temperature dependence of the isotherms and the maximum capacity independently.

Table 6 – Sips isotherm parameters, average heats of adsorption and LDF coefficients for CO₂, CO, N₂, CH₄ and H₂ on zeolite 13X.

Component	unit	CO ₂	CO	N ₂	CH ₄	H ₂
$A_{1,i}$	[mol/kg]	8.984	9.614	6.774	13.69	8.519
$A_{2,i} \times 10^3$	[mol/(kg K)]	-9.867	-19.27	-11.57	-31.67	-13.57
$B_{0,i} \times 10^6$	[kPa ⁻¹]	2.266	13.95	3.778	38.36	5.651
$B_{0,i}$	[K]	3130	1496	1650	1083	640
$C_{1,i} \times 10^2$	[-]	36.22	-14.61	76.74	66.51	95.91
$C_{2,i}$	[K]	454.4	407	78.83	97.8	9.776
ΔH_i^{iso}	[J/mol]	37000	25000	19000	19000	8050
ΔH_i^{iso} Upper bound	[J/mol]	52000	35000	21000	21000	8200
ΔH_i^{iso} Lower bound	[J/mol]	31000	22000	18000	18000	7800
k_i	[1/s]	0.1	0.7	1.6	0.9	1.6

3.2 Base case cycle performance

The base case was chosen based on an optimization of the cycle shown in Figure 2 for a steam methane reformer syngas after the high temperature water-gas shift (HT-WGS) reactor that has been cooled to around 35 °C and dried. The specifications are reported in Table 7 [2]. The same stream has been examined in D1.1.1 [3].

Table 7 – VPSA inlet stream specifications (dry) typical for a steam methane reforming process including a HT-WGS [2].

H ₂	CO ₂	CH ₄	CO	N ₂	P	T
[Vol%]	[Vol%]	[Vol%]	[Vol%]	[Vol%]	[bar]	[°C]
75.81	16.31	3.03	4.65	0.2	25	35

The performance reached for this cycle is reported in Table 8 below. In addition to the separation performance indicators purity and recovery, the productivity is a commonly used indicator for the capital cost and related to the adsorbent inventory necessary for a

certain production rate. It is defined as the amount of product N_{Prod} obtained per unit time t_{cycle} and unit mass of adsorbent m_{ads} :

$$Pr = \frac{N_{\text{Prod}}}{t_{\text{cycle}} m_{\text{ads}}} \quad (1)$$

Table 8 – Values of performance indicators for reference cycle simulation for the inlet stream reported in Table 7 and the cycle shown in Figure 2.

H ₂ purity	H ₂ recovery	CO ₂ purity	CO ₂ recovery	productivity
[%]	[%]	[%]	[%]	[kgCO ₂ /t _{ads} /h _{cycle}]
99.981	91.88	96.67	95.32	197.4

All results of the sensitivity analysis are given as ratio between the new value of the key performance indicator and the value obtained for the base case.

3.3 Sensitivity analysis on mass transfer coefficient

The results of the sensitivity analysis on the mass transfer coefficient are shown in Figure 3. The figure shows how the most important performance indicators vary for double and half the mass transfer coefficient k_i compared to the base case reported in Table 6. For all performance indicators, the figure shows the furthest left the base case and to the right the variations for first the upper bound (twice the mass transfer), then the lower bound (half the mass transfer) for CO₂, CO, CH₄, N₂ and H₂, and finally for varying all of them together. The dashed black line indicates the base case. The red and blue lines indicate the boundaries above which the targeted separation performance can still be achieved, that is H₂ purity > 99.97 %, H₂ recovery > 90 %, CO₂ purity > 96 % and CO₂ recovery > 90 %. Because of the high purity requirements for H₂, the changes are shown on a different axis (left axis in blue for H₂, right axis in red for all others) to appreciate even small differences.

It is evident from the figure that changing the mass transfer of CO₂ has the most pronounced effect on the separation performance and the productivity among all the components. For a high mass transfer coefficient, the CO₂ purity decreased below the threshold, which can be understood as follows: because of a steeper CO₂ front during adsorption and heavy purge (HP), at the end of the HP step the CO₂ front is further from the end of the column, which is therefore still contaminated with more impurities. For a low mass transfer, the H₂ purity decreases below the threshold because the CO₂ front propagates further through the column during the HP step thereby contaminating it more and pushing the other impurities further ahead. For both cases, shortening (for the case of a slower mass transfer) or extending (for the case of a faster mass transfer) the adsorption step or reducing (slow mass transfer) or increasing (fast mass transfer) the recycle ratio are easy means to still obtain the required separation performance. This means that even if the mass transfer coefficient for CO₂ has been over- or underestimated for process optimization, the results can still be used and the process can be adjusted easily to obtain the required separation performance by slightly varying a single process parameter (adsorption time or recycle ratio).

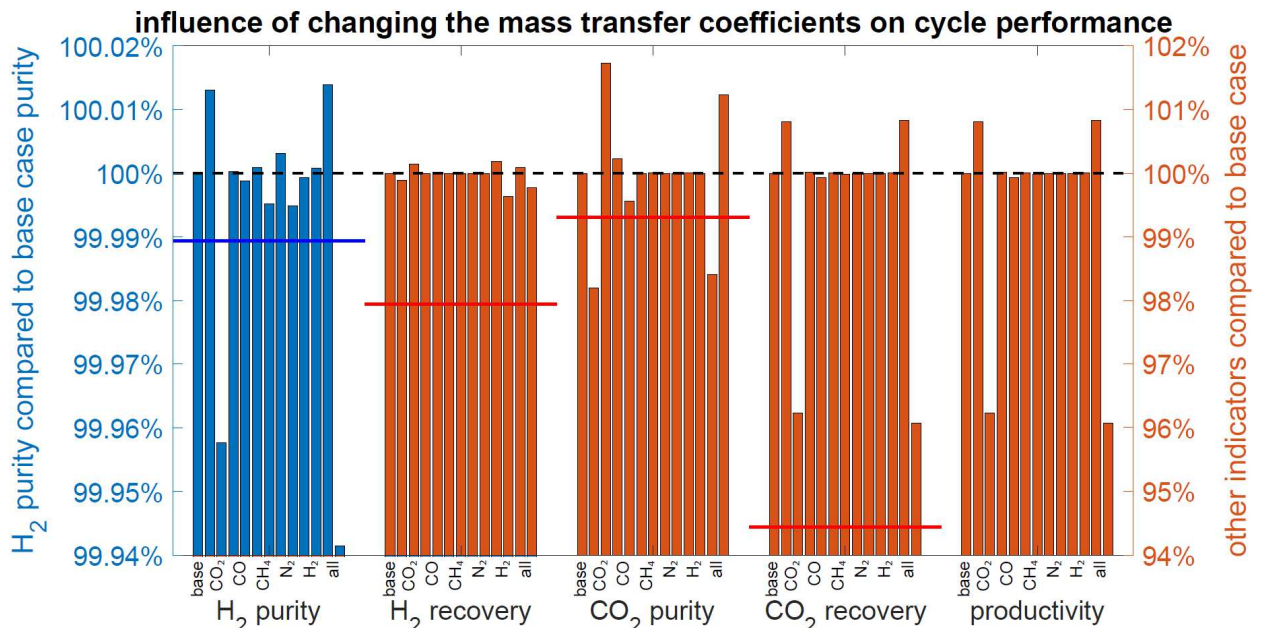


Figure 3 – Sensitivity of performance indicators when changing the mass transfer coefficient. The graph shows the ratio of the performance indicators purity (CO₂ and H₂), recovery (CO₂ and H₂) and productivity between the case of a varied mass transfer coefficient and the base case. The graph shows for all components first the case of a higher mass transfer coefficient (twice that of the base case) and then the case of a lower mass transfer coefficient (half that of the base case). The blue and red lines indicate the boundaries for 99.97 % H₂ purity, 90 % H₂ recovery, 96 % CO₂ purity and 90 % CO₂ recovery. Above those lines, the respective separation target is reached. The black dotted line corresponds to the base case.

For all components other than CO₂, even when doubling or halving the mass transfer coefficient, the separation performance and the productivity do not change significantly. When changing all parameters together, the effect is governed by the effect of the CO₂ mass transfer coefficient. It can thus be concluded that an accurate estimation of the CO₂ mass transfer coefficient is important, whereas less accuracy is needed for the mass transfer coefficient of the other components. This is due to adsorption and desorption being governed mainly by heat transfer and the temperature in the bed rather than by mass transfer limitations, as mentioned before and explained further in literature [12].

3.4 Sensitivity analysis on heat of adsorption

Whereas the heat transfer from the bed to the surrounding is setup specific and can be neglected for large scale industrial columns (close to adiabatic operation), the heat of adsorption is a parameter that depends on the adsorbate and adsorbent used and can be determined from isotherm measurements. The heat of adsorption depends on loading and temperature. However, for process modelling a loading and temperature independent heat of adsorption representative for the temperatures and loadings of interest is used. The upper and lower boundaries for the sensitivity analysis are reported in Table 6 and based on the boundaries for low loadings (high heat of adsorption) and high loadings (low heat of adsorption) as reported by Park et al. [16]. The results of the sensitivity analysis are illustrated in Figure 4. The figure shows how the most important performance indicators vary for a high and low heat of adsorption. For all performance

indicators, the figure shows the base case to the left and to the right the variations for first the high and after the low heat of adsorption for CO₂, CO, CH₄, N₂ and H₂ and finally for varying all together. The dashed black line indicates the base case. The red and blue lines indicate the boundaries above which the targeted separation performance can still be achieved for the respective purity or recovery.

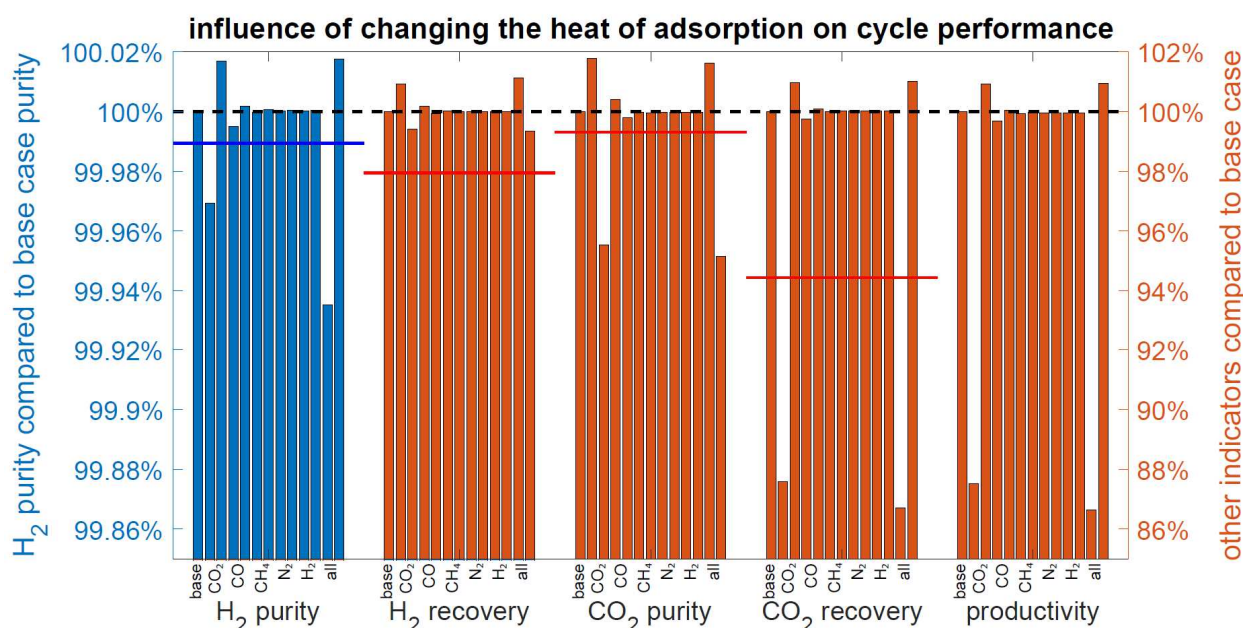


Figure 4 – Sensitivity of performance indicators when changing the heat of adsorption. The graph shows the ratio of the performance indicators purity (CO₂ and H₂), recovery (CO₂ and H₂) and productivity between the case of a varied heat of adsorption and the base case. The graph shows for all components first the case of a higher heat of adsorption and then of a lower heat of adsorption with the values reported in Table 6. The blue and red lines indicate the boundaries for 99.97 % H₂ purity, 90 % H₂ recovery, 96 % CO₂ purity and 90 % CO₂ recovery. Above those lines, the respective separation target is reached. The black dotted line corresponds to the base case.

As for the mass transfer coefficient, also for varying the heat of adsorption the influence of CO₂ is the strongest. This is the case i) because of the high concentration of CO₂ in the feedstream, ii) because of the high heat of adsorption and iii) because of the boundaries for low and high loadings, which relate to a change in heat of adsorption of almost 50 %. A high heat of adsorption leads to a process with higher temperature variations, which is unfavourable for the separation and translates into a lower H₂ purity. This is because the column is at higher temperature during adsorption, which is related to less CO₂ and impurities being adsorbed and therefore a faster propagation of the fronts and an earlier breakthrough. This also relates to an earlier breakthrough of CO₂ during the HP, thereby leading to lower CO₂ recoveries. For a lower heat of adsorption, the CO₂ purity is insufficient because of a stronger adsorption of CO₂ and a slower propagation of the front at lower temperatures during the adsorption and HP steps. Therefore, impurities are still present at the column top after the HP. To achieve the separation performance it is sufficient to either shorten (high heat of adsorption) or extend (low heat of adsorption) the adsorption step or to reduce (high heat of adsorption) or increase (low heat of

adsorption) the recycle ratio, as explained for the mass transfer coefficient in the previous section. For all other components, the effect is small mainly because they either have a very low heat of adsorption together with little adsorption (case of H₂), or are only present in small amounts in the feed gas (case of the other components). When changing all parameters together, the effect is governed mainly by the effect of the heat of adsorption of CO₂.

Therefore, also for the heat of adsorption, determining it for CO₂ is very important, whereas an approximate value for the other components does not influence the outcome of process optimizations significantly. For CO₂, however, making sure that the heat of adsorption is taken for the loadings relevant for the application is critical. This means e.g. that for a process in which the column is never fully regenerated but only up to a certain loading, the average of the isosteric heat should not include lower loadings, whereas for a breakthrough experiment, it should.

3.5 Sensitivity analysis on adsorption isotherms

Knowing the adsorption isotherms is essential for designing adsorption processes. However, often adsorption isotherms are only available for a limited range of pressures and/or temperatures, or isotherms for specific components are missing. In addition, isotherm measurements are not 100 % accurate and the mathematical description with a fitted empirical isotherm adds additional errors. Moreover, especially at an early stage of material development, the material is available in pure form as powder only rather than pelletized. Whereas pelletization is needed to reduce the pressure drop during an adsorption process (for fixed beds) and critical for mechanical stability, it reduces the capacity of the material because the pellets are composed of binder and adsorbing material and not of pure adsorbing material. Here, the influence of two specific cases on the performance indicators of a VPSA process is shown: a case w/o temperature dependence and a case with a changed maximum capacity.

3.5.1 No temperature dependence of adsorption isotherms

For the first case, the temperature dependence of the adsorption isotherms was eliminated assuming that the isotherms are known for the feed temperature (here: 35 °C). Having isotherm measurements only at one specific temperature results on the one hand in not being able to describe the adsorption behavior accurately during a non-isothermal process. On the other hand, this usually also relates to an additional assumption for the heat of adsorption, because isotherms at various temperatures are needed to compute the heat of adsorption (see section 2.1.2). The results of the sensitivity analysis are illustrated in Figure 5 showing the change in performance indicators when eliminating the temperature dependence of the isotherms. The figure shows for every performance indicator first the base case and to the right the cases without temperature dependence of the isotherms for CO₂, CO, CH₄, N₂ and H₂ and finally for removing the temperature dependence for all isotherms. The dashed black line indicates the base case. The red and blue lines indicate the boundaries above which the targeted separation performance can still be achieved.

The figure shows that not accounting for any temperature dependence changes the results more than varying the mass transfer (section 3.3) or the heat transfer (section 3.4) coefficient. The separation target is not reached when eliminating the temperature

dependence for CO₂, CO or N₂. For CO₂, the CO₂ purity drops by over 15 %. This is due to a stronger adsorption of CO₂, which therefore leaves the column unsaturated in CO₂ after the HP step. This would, however, lead to a process improvement, because the adsorption time could be increased. This becomes clear when looking at the increase in H₂ purity for eliminating the *T*-dependence of CO₂. For a temperature independent CO isotherm, the CO₂ purity drops by over 2.5 % compared to the base case, because a stronger adsorption of CO leads to its front being closer to the CO₂ front during the HP, thereby making them more difficult to separate. For a temperature independent N₂ isotherm, the H₂ purity drops by over 0.05 %, which is significant when targeting purities > 99.97 %. The effect is magnified when eliminating the temperature dependence for all isotherms together.

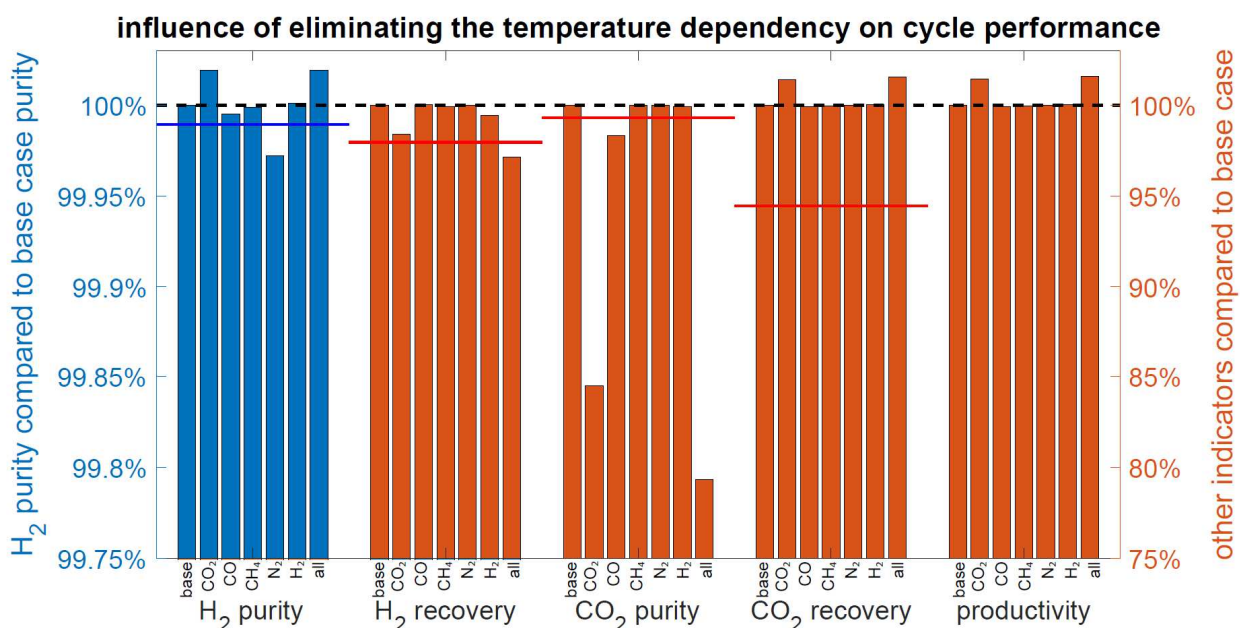


Figure 5 – Sensitivity of performance indicators when eliminating the temperature dependence of the adsorption isotherms and using isotherm values for the feed temperature (35 °C). The graph shows the ratio of the performance indicators purity (CO₂ and H₂), recovery (CO₂ and H₂) and productivity between the case of no temperature dependence and the base case. The blue and red lines indicate the boundaries for 99.97 % H₂ purity, 90 % H₂ recovery, 96 % CO₂ purity and 90 % CO₂ recovery, above those lines the specific indicator still reaches the separation target. The black dotted line corresponds to the base case performance.

However, both for CH₄ and for H₂, the effect of using temperature independent isotherms is negligible. For CH₄, the influence is low because the propagation velocity of the CH₄ front is in between the one of the CO front (closer to the CO₂ front) and the one of the N₂ front (closer to the H₂ front). Therefore, even if methane propagates faster, it will still not break through before N₂ and affect the H₂ purity, and if it propagates slower, it will only have a minor impact on the CO₂ purity, because it moves ahead of the CO front. For H₂, eliminating the *T* dependence has no significant impact on the process performance because of its low adsorption in general compared to all other components.

From these considerations, it is clear that it is essential to know the temperature dependent isotherms for CO₂, for the leading impurity front (here N₂) and for the impurity

front which is closest to CO₂ (here CO). The impact of an impurity which propagates at intermediate velocity with another front in between CO₂ and the impurity (here CO), as well as between the impurity and H₂ (here N₂), is less pronounced. Depending on the exact process and case study, not having a temperature dependent isotherm might be sufficient for predictive process modelling. In a three component system with CO₂, CH₄ and H₂, however, CH₄ would both be the leading impurity front as well as the one closest to CO₂, therefore the temperature dependence of the isotherm can be expected to have a high impact on the process performance and should not be neglected. In addition, which impurity front moves the fastest and the slowest also depends on the feedstream composition as well as the process temperatures and pressures. Therefore, this assessment might change for different feedstreams, e.g. for an ATR rather than an SMR or when adding a low-temperature WGS reactor to the process flowsheet, and for different process conditions. Furthermore, it is – of course – adsorbent dependent, because different adsorbents feature different adsorption strengths for the different components.

However, having the temperature dependence of the light component, as long as it features a very low adsorption capacity, seems unnecessary. Therefore, we have chosen to not always measure the H₂ isotherm at different temperatures – especially because also changing the heat of adsorption related to H₂ adsorption and desorption does not affect the performance significantly, as discussed in section 3.4.

3.5.2 Maximum capacity

The second case examined for the adsorption isotherms is one where the temperature invariant part of the maximum capacity ($A_{1,i}$) is changed by $\pm 10\%$ compared to the base case. The results of the sensitivity analysis are illustrated in Figure 6, which shows the variation of the most important performance indicators for a higher and lower adsorption capacity compared to the base case. For all performance indicators, the figure shows first the base case to the left, and to the right the variations for first the high (10% increase) and after the low (10% decrease) adsorption capacity. The results are shown first for CO₂ followed by CO, CH₄, N₂ and H₂ and after for varying all of them together. Lastly, a case where H₂ adsorption is set to zero is shown. The dashed black line indicates the base case. The red and blue lines indicate the boundaries above which the targeted separation performance can still be achieved.

The figure shows that the effect on the H₂ purity, the CO₂ recovery and the productivity is stronger than for eliminating the temperature dependence of the adsorption isotherms, whereas the effect on the H₂ recovery is comparable and the effect on the CO₂ purity is less pronounced. As for eliminating the temperature dependence, also in this case some components have a major influence, whereas others do not.

First, one can see that changing the capacity of the H₂ isotherm does barely affect the performance indicators and the target separation performance is reached in all cases with changes below 0.2% for all indicators and even below 0.004% for H₂ purity. This motivated an additional study in which the H₂ adsorption was eliminated (case indicated as *noH₂* in Figure 6). When H₂ does not adsorb, only the H₂ recovery is below the threshold (which can be changed by slightly increasing the adsorption duration) with the other indicators changing less than 1% (and less than 0.02% for H₂ purity). This underlines what has been suggested in the previous section: an accurate determination

of the hydrogen isotherm is not essential, as long as it can be guaranteed that its adsorption is significantly weaker than the adsorption of any other adsorbent. It should, however, be highlighted, that this can be different if impurities with a very low adsorption affinity like Ar are present in the feedstream, which is the case for example for H₂ rich streams originating from ATR of natural gas.

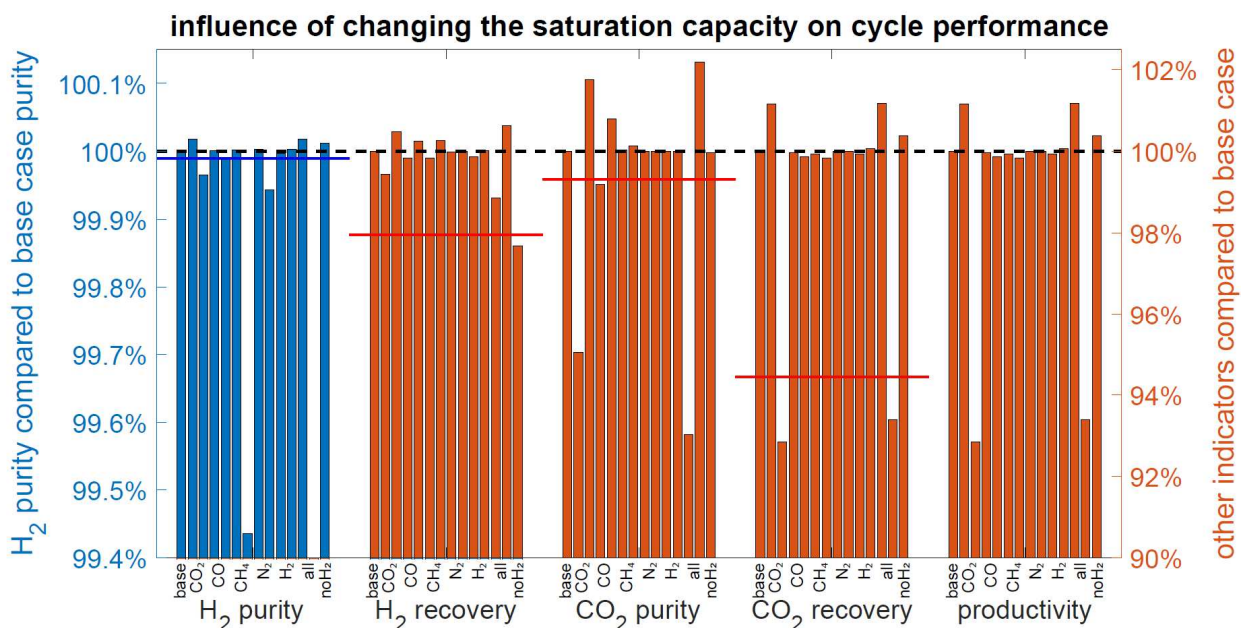


Figure 6 – Sensitivity of performance indicators when changing the adsorption capacity. The graph shows the ratio of the performance indicators purity (CO₂ and H₂), recovery (CO₂ and H₂) and productivity for the case of a varied adsorption capacity to the base case w/o variation. The graph shows for all components first the case of a higher adsorption capacity (+ 10 %) and then of a lower adsorption capacity (– 10 %). ‘NoH₂’ indicates a case where zero H₂ adsorption is assumed. The blue and red lines indicate the boundaries for 99.97 % H₂ purity, 90 % H₂ recovery, 96 % CO₂ purity and 90 % CO₂ recovery. Above those lines, the respective separation targets are reached. The black dotted line corresponds to the base case.

Second, it is clear that also in this case, the CO₂ isotherm has the most significant effect: decreasing the CO₂ adsorption capacity by 10 % leads to several performance indicators falling below the threshold (H₂ purity, CO₂ recovery) and to a drop in productivity by almost 10 %. Increasing it results in a decreased CO₂ purity with the reasoning being the same as for an elimination of the temperature dependence.

Changing the adsorption capacity of CO, N₂ and CH₄ also results in not meeting the performance requirements. For CO, interestingly, decreasing its capacity does not affect the performance as much and all indicators are above the set threshold. In this case, the front propagates faster, which leads to an earlier breakthrough, but because it is not the leading impurity front, the effect is small. The effect of CH₄ now is relevant as well, because by decreasing its capacity, its front will now propagate so fast that it starts breaking through at a similar time as nitrogen does thereby contaminating the H₂ product.

3.6 Summary of sensitivity analysis

The sensitivity analysis has shown that whereas changing the mass transfer rate has very little influence on the performance indicators, the effect is more pronounced for changing the heat of adsorption. This is because the heat of adsorption is high for CO₂ and therefore the rate of adsorption is governed by the temperature decrease or increase rather than by the mass transfer rate. In both cases, the influence of CO₂ is the largest thus leading the one or more performance indicators to fall below the threshold for the separation requirements of 99.97 % H₂ purity and 96 % CO₂ purity, at 90 % recovery for both. For all other components, the change in separation performance is minor and the separation target can still be met. Therefore, whereas an accurate determination of the mass transfer rate and the heat of adsorption is critical for CO₂, for the other components this is less crucial.

Changing the isotherm parameters or eliminating the temperature dependence of the adsorption isotherms has a more pronounced effect on the separation performance indicators with most variations resulting in the separation target not being met any longer and several indicators decreasing by over 20 %. This demonstrates that an accurate measurement of the isotherms at various temperatures is essential not only for CO₂, but also for the impurities, especially for the leading impurity front (here N₂) and for the impurity front which propagates the slowest, hence it is the most likely to contaminate the CO₂ product. For H₂, however, knowing the isotherm is not as important and not knowing its temperature dependence does not change the results of the simulation significantly, as long as its adsorption is much weaker than that of any other component. Even assuming no hydrogen adsorption at all is a reasonable assumption.

4 COMMERCIAL ADSORBENTS

Whereas there has been a significant effort in developing novel adsorbent materials, commercially available adsorbent like zeolites or activated carbons still should be the starting point for the design of a new adsorption process. The best commercial adsorbents often outperform most novel sorbent materials, as shown by Balashankar et al. for the case of vacuum swing adsorption for post-combustion CO₂ capture [17]. For H₂ purification, the most common adsorbents are zeolites and activated carbons or layered beds using a combination thereof [18]. Those adsorbent materials also show promise for CO₂ capture, because they feature a strong adsorption of CO₂.

4.1 Zeolite 13X

Zeolite 13X has been identified as the best performing adsorbent for CO₂-H₂-impurity separation in the context of coupling H₂ production with carbon capture [3]. Its commercial availability and low cost make it a good choice for a technology which has to be cost competitive and advance quickly to high technology readiness levels (TRL).

4.1.1 Adsorption isotherms

The measured adsorption isotherms on CH₄, Ar and H₂ together with the fitted temperature dependent Sips isotherm equation are shown in Figure 7. The corresponding isotherm parameters are reported in Table 9.

Table 9 – Sips parameters for CH₄, Ar and H₂ on zeolite 13X. For the sake of completeness, also the parameters for CO₂ and N₂ from previous measurements on the same material are included [19].

		CH ₄	Ar	H ₂	CO ₂	N ₂
T_{ref}	[K]	298.15	298.15	298.15	298.15	298.15
$a_{1,i}$	[mol/kg]	4.7159	5.6811	9.7409	7.286	4.051
$a_{2,i}$	[-]	-1.1462	0	0	-0.06168	0
$b_{0,i}$	[bar ⁻¹]	5.80e-4	1.12e-4	3.99e-5	1.13e-4	5.85e-5
$b_{1,i}$	[kJ/mol]	14.280	13.245	9.6101	28.389	18.474
$c_{1,i}$	[-]	0.99020	1.0363	0.94888	0.42456	0.98624
$c_{2,i}$	[-]	0.71740	-2.08e-1	0	0.72378	0

Whereas CH₄ features a strong affinity and seems to approximate its maximum adsorption capacity at 30 bar, the H₂ isotherm is linear up to 30 bar with a much lower capacity. The affinity towards Ar is significantly lower than for CH₄, but still higher than for H₂ and the isotherms are flattening already significantly at pressures below 30 bar. The Sips isotherm equation can fit all isotherms very well.

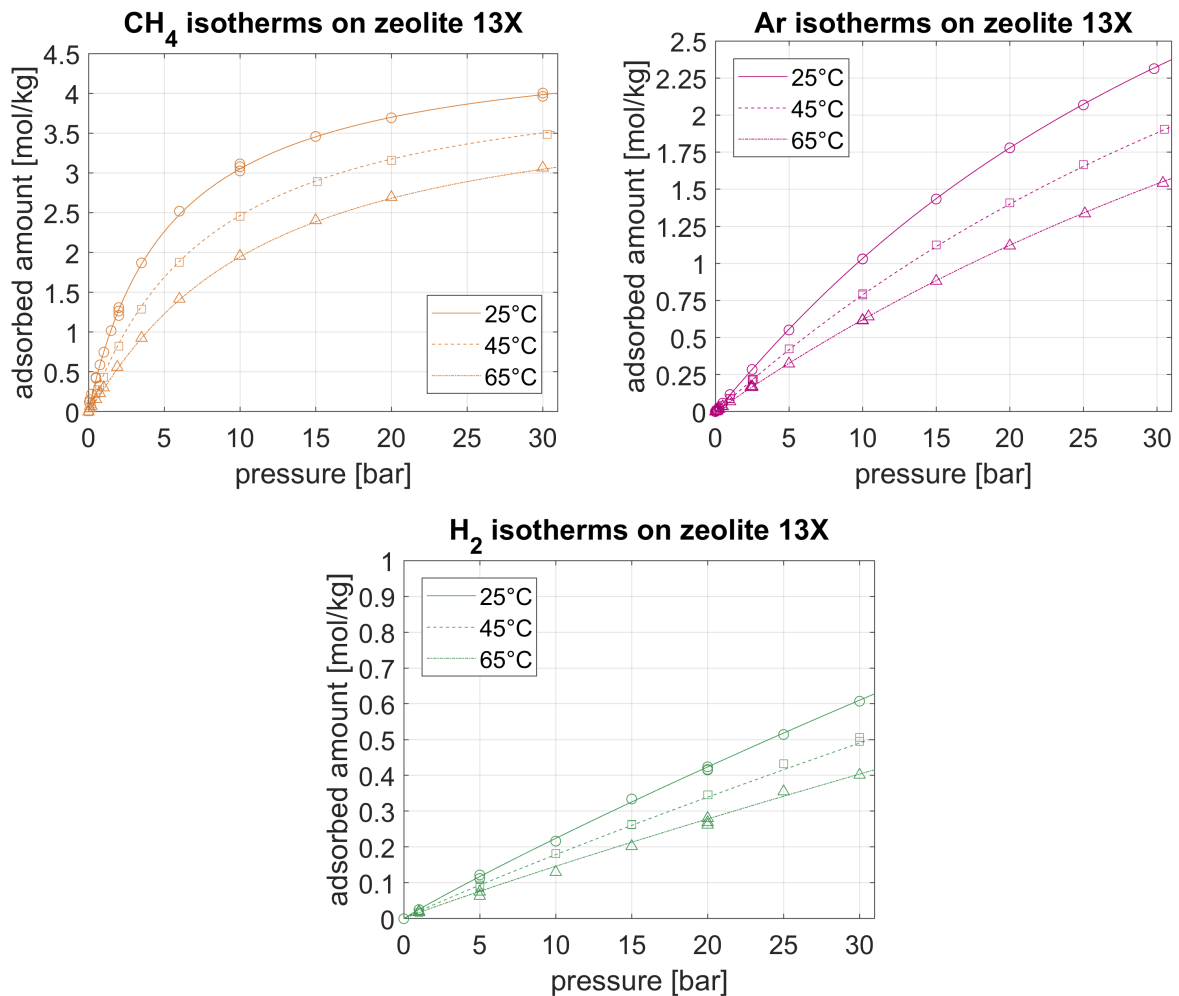


Figure 7 – Measured isotherms on zeolite 13X at 25 °C (circles), 45 °C (squares) and 65 °C (triangles) for different gases (CH₄, Ar and H₂), the fitted temperature dependent Sips isotherms are shown as lines with the respective isotherm parameters being reported in Table 9.

A comparison with other materials showing also the CO₂ and N₂ adsorption will follow in section 6.

4.1.2 Isostatic heat of adsorption

The heats of adsorption on zeolite 13X averaged over all three temperatures are shown in Figure 8. The strong affinity towards CH₄ is supported by the high heat of adsorption at low loadings, which decreases for higher loadings but is still significantly higher than for both Ar and H₂. The latter feature a low heat of adsorption showing that the interaction between Ar and H₂ and zeolite 13X is weak.

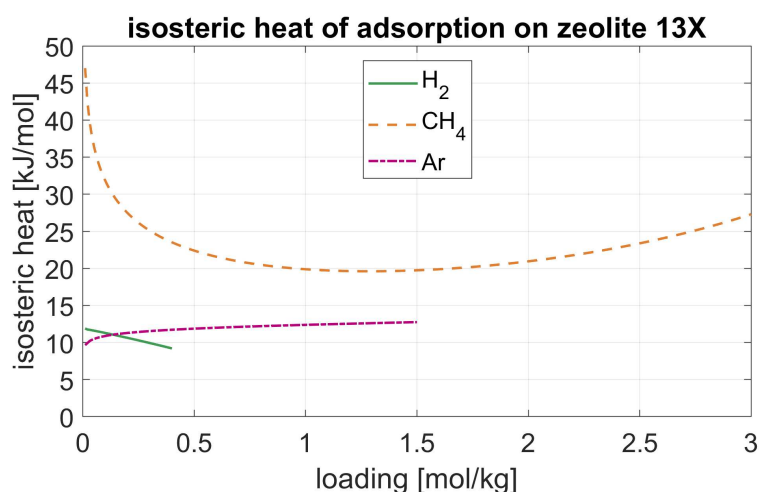


Figure 8 – Isostatic heat of adsorption for H_2 , CH_4 and Ar on zeolite 13X for different loadings averaged over temperature (25, 45 and 65 °C). Only the loadings up to which measurements for all three temperatures were available were considered for the evaluation.

4.2 Breakthrough experiments

Both binary and ternary breakthrough experiments were performed on pelletized zeolite 13X. The reproducibility of the experiments was controlled by comparing i) repetitions of the same experiment in the same column and ii) the same experiment performed in different columns. The reproducibility in the same column was excellent and slightly worse but still satisfactory when performing the same experiment in two different columns, as discussed in more detail in section 4.2.1.2. The estimation of the mass transfer coefficients was difficult and somewhat inconclusive due to a high heat of adsorption of CO_2 on zeolite 13X. The shape of the breakthrough is therefore determined by heat transfer rather than by mass transfer. This is in line with the literature [12].

4.2.1 Binary breakthrough experiments

The binary breakthrough experiments were performed for a mixture of 50 mol% CO_2 and 50 mol% CH_4 . A typical breakthrough experiment is shown in Figure 9 for a pressure of 10 bar, a temperature of 25 °C, a feed flowrate of 20 cm^3/s and fixed transport parameters $k_{He} = 1 s^{-1}$, $k_{CO_2} = 0.1 s^{-1}$ and $k_{CH_4} = 0.5 s^{-1}$. The temperatures inside the column at five different locations as indicated in Table 10 are shown at the top and the composition measured after the column at the bottom. The symbols indicate the experimental points and the lines are the simulation results for the same experiment whilst fitting the feed velocity (to account for errors inherent to the MFCs) and the internal heat transfer coefficient.

Table 10 – Location of the different thermocouples.

Thermocouple	T11	T12	T13	T14	T15
Distance from column bottom [m]	0.1	0.35	0.6	0.85	1.1

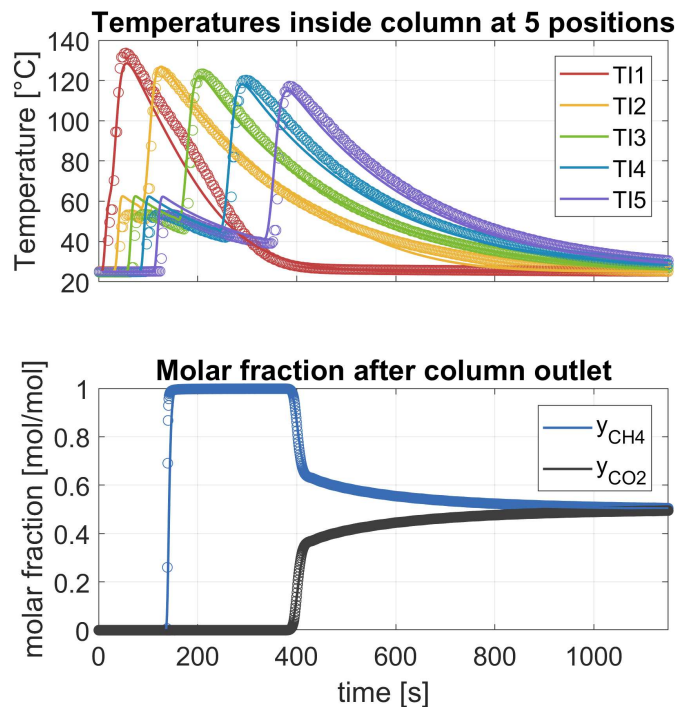


Figure 9 – Breakthrough experiment for a mixture of 50 mol% CO_2 and 50 mol% CH_4 at a pressure of 10 bar, a temperature of 25 °C and a feed flowrate of 20 cm³/s. The circles indicate experimental points and the lines indicate the modelling results. The linear driving force coefficients are fixed to $k_{He} = 1 \text{ s}^{-1}$, $k_{CO_2} = 0.1 \text{ s}^{-1}$ and $k_{CH_4} = 0.5 \text{ s}^{-1}$ and the internal heat transfer coefficient $h_c = 25.2 \frac{W}{m^2K}$ is fitted to the individual experiment.

Due to the lower adsorption capacity, the methane front propagates faster through the column. During CH_4 adsorption, heat is released and a front of a moderate temperature increase around 40 K propagates through the column. After approximately 150 s and shortly after the temperature front reaches the thermocouple closest to the column top (TI5), CH_4 breakthrough can be observed. Pure CH_4 is produced for around 250 s before CO_2 starts breaking through. CO_2 adsorbs significantly more and has a higher heat of adsorption. This results in a front of very high temperatures up to 130 °C propagating much slower through the column than the CH_4 temperature front. After the maximum temperature is reached at any point in the column, the temperature decreases slowly. As the temperature goes down, more CO_2 adsorbs, which releases more heat. Therefore, whereas the initial part of the CO_2 breakthrough is a sharp front, it has a long tail and it takes a long time – until the column reaches a stable temperature – until the composition at the column outlet reaches the feed concentration.

The model can reproduce the breakthrough profiles very well, both for the temperature and for the concentration profiles, by capturing the moderate temperature increase related to methane adsorption, the high temperature peaks related to CO_2 adsorption and the slow decrease in temperature together with the long tail of the concentration profile after CO_2 breakthrough until the feed composition is reached.

4.2.1.1 Mass transfer

The mass transfer of He was found to be fast and not to influence the results, as long as a high value was chosen. We therefore fixed $k_{\text{He}} = 1 \text{ s}^{-1}$, which worked well for all experiments. When estimating k_{CH_4} , a value in the range of 0.4 s^{-1} to 0.6 s^{-1} performed the best with 0.5 s^{-1} being a good compromise with good fits for all experiments. Therefore, we subsequently fixed $k_{\text{CH}_4} = 0.5 \text{ s}^{-1}$. For CO_2 , linear driving force coefficients between 0.05 s^{-1} and 0.5 s^{-1} did result in good fits with little sensitivity. In the following, we therefore also assessed two cases with a fixed value for k_{CO_2} . The first with $k_{\text{CO}_2} = 0.25 \text{ s}^{-1}$ and the second with $k_{\text{CO}_2} = 0.1 \text{ s}^{-1}$ to be consistent with Marx et al. [12]. The comparison of these three fits is shown for the same experiment as before (10 bar, $25 \text{ }^\circ\text{C}$, $20 \text{ cm}^3/\text{s}$) in Figure 10 below. The dashed lines are for fitted $k_{\text{CO}_2} = 0.235 \text{ s}^{-1}$, the dotted lines for a fixed $k_{\text{CO}_2} = 0.25 \text{ s}^{-1}$ and the solid lines for a fixed $k_{\text{CO}_2} = 0.1 \text{ s}^{-1}$ as shown also in Figure 9.

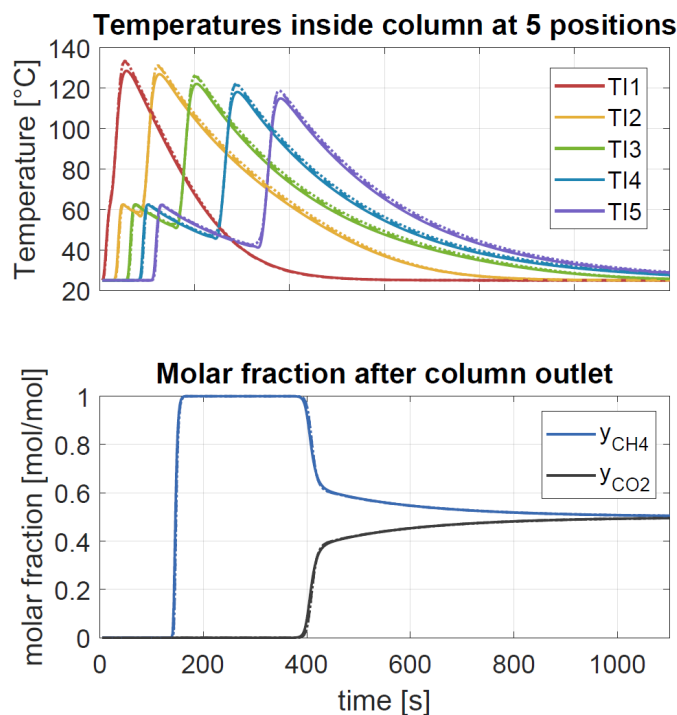


Figure 10 – Fitting of breakthrough experiment for a mixture of 50 mol% CO_2 and 50 mol% CH_4 at a pressure of 10 bar, a temperature of $25 \text{ }^\circ\text{C}$ and a feed flowrate of $20 \text{ cm}^3/\text{s}$. The linear driving force coefficients are fixed to $k_{\text{He}} = 1 \text{ s}^{-1}$ and $k_{\text{CH}_4} = 0.5 \text{ s}^{-1}$. The dashed lines indicate the case where k_{CO_2} is optimized and the best fit is obtained for $k_{\text{CO}_2} = 0.235 \text{ s}^{-1}$, the dotted lines indicate the case with $k_{\text{CO}_2} = 0.25 \text{ s}^{-1}$ the solid lines the case with $k_{\text{CO}_2} = 0.1 \text{ s}^{-1}$ as shown already in comparison to the experimental results in Figure 9. The internal heat transfer coefficient is fitted individually to each of the three cases with $h_c = 24.5, 24$ and $25.2 \text{ W}/(\text{m}^2\text{K})$ for the fitted k_{CO_2} , $k_{\text{CO}_2} = 0.25 \text{ s}^{-1}$ and $k_{\text{CO}_2} = 0.1 \text{ s}^{-1}$ respectively.

It can be seen that even when fixing the mass transfer coefficient of CO_2 to very different values, the fit is very similar. There is a slight decrease in the height of the temperature peaks related to CO_2 adsorption when a low $k_{\text{CO}_2} = 0.1 \text{ s}^{-1}$ is chosen and the breakthrough is a little less sharp. The estimation of the heat transfer coefficient is

insensitive to changing the mass transfer with $h_C = 24.5$, 24 and 25.2 W/(m²K) for the fitted k_{CO_2} , $k_{CO_2} = 0.25 \text{ s}^{-1}$ and $k_{CO_2} = 0.1 \text{ s}^{-1}$ respectively.

Moreover, for all other binary breakthrough experiments at different temperatures and pressures, there is only an insignificant difference when varying the linear driving force coefficient for CO₂ within those boundaries. Each coefficient could describe the experiment similarly well. The other breakthrough experiments are shown in Figure 11, Figure 12, Figure 13 and Figure 14 for different pressures and temperatures and different columns for the case of a mass transfer coefficient $k_{CO_2} = 0.1 \text{ s}^{-1}$. Overall, the agreement between experiments and simulations is satisfactory. We therefore suggest using constant mass transfer coefficients independent of temperature or pressure for modelling adsorption processes. To be consistent with the literature [12] and as a conservative approach, we will use a value of $k_{CO_2} = 0.1 \text{ s}^{-1}$ for the ternary breakthrough experiments.

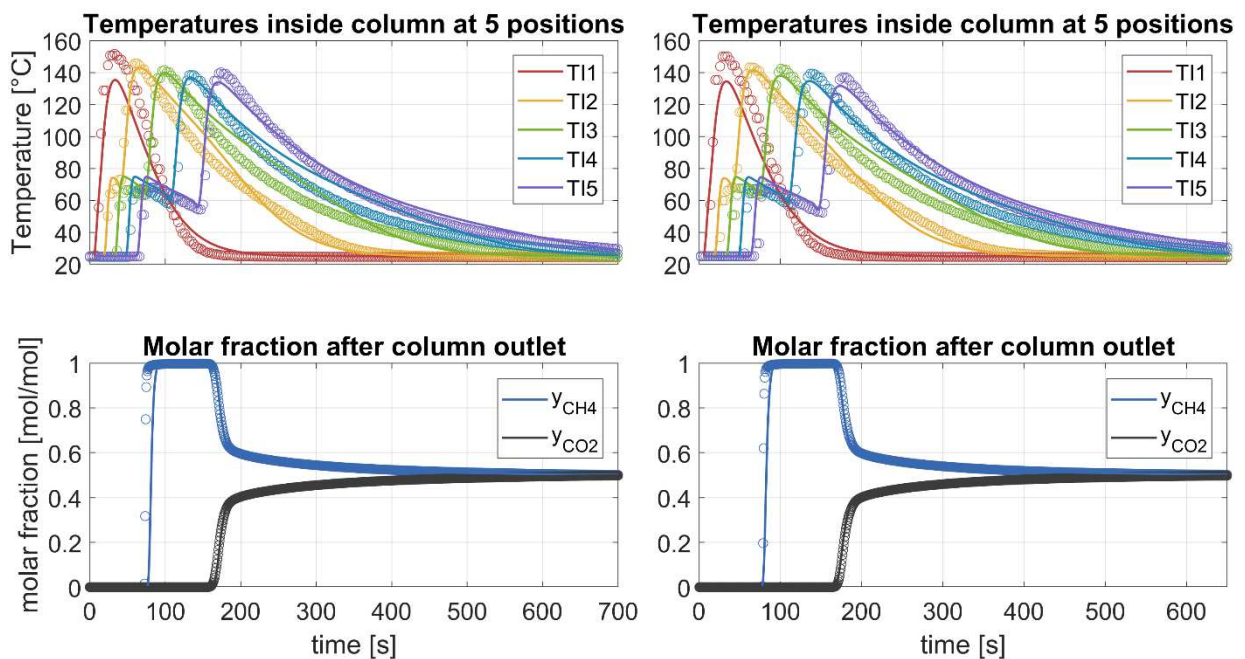


Figure 11 – Breakthrough experiments for a mixture of 50 mol% CO₂ and 50 mol% CH₄ at a pressure of 25 bar, a temperature of 25 °C and a feed flowrate of 20 cm³/s. The circles indicate experimental points and the lines indicate the modelling results. The linear driving force coefficients are fixed to $k_{He} = 1 \text{ s}^{-1}$, $k_{CO_2} = 0.1 \text{ s}^{-1}$ and $k_{CH_4} = 0.5 \text{ s}^{-1}$ and the internal heat transfer coefficient is fitted to the individual experiment. Left: column 1, right: column 2.

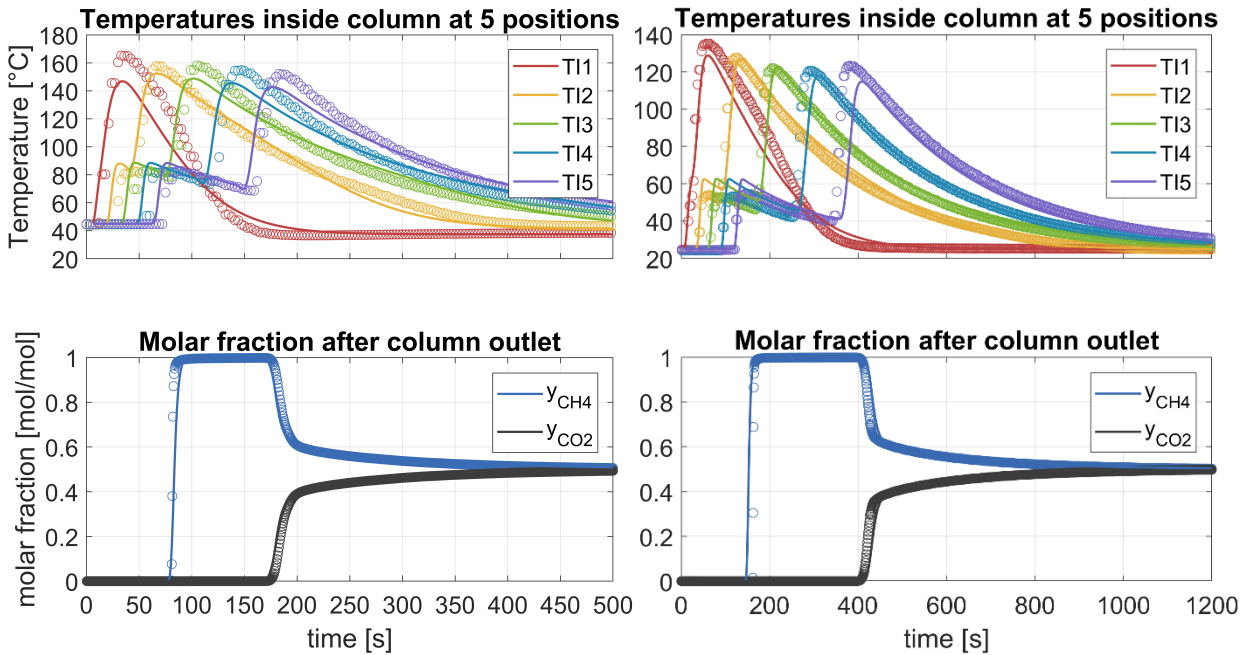


Figure 12 – Breakthrough experiments for a mixture of 50 mol% CO₂ and 50 mol% CH₄. Left: pressure of 25 bar, temperature of 45 °C, feed flowrate of 20 cm³/s, column 2. Right: pressure of 10 bar, temperature of 25 °C, feed flowrate of 20 cm³/s, column 1. The circles indicate experimental points and the lines indicate the modelling results. The linear driving force coefficients are fixed to $k_{He} = 1 \text{ s}^{-1}$, $k_{CO_2} = 0.1 \text{ s}^{-1}$ and $k_{CH_4} = 0.5 \text{ s}^{-1}$ and the internal heat transfer coefficient is fitted to the individual experiment.

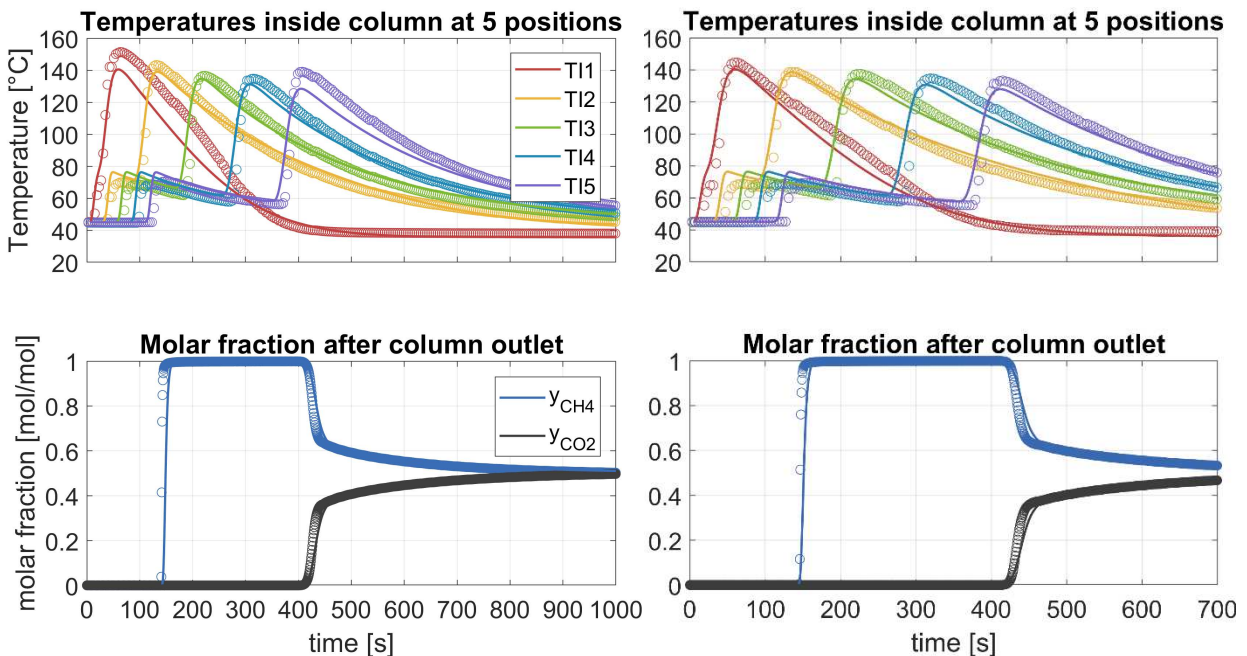


Figure 13 – Breakthrough experiments for a mixture of 50 mol% CO₂ and 50 mol% CH₄ at $P = 10 \text{ bar}$, $T = 45 \text{ °C}$ and feed flowrate of 20 cm³/s. The circles indicate experimental points and the lines indicate the modelling results. The linear driving force coefficients are fixed to $k_{He} = 1 \text{ s}^{-1}$, $k_{CO_2} = 0.1 \text{ s}^{-1}$ and $k_{CH_4} = 0.5 \text{ s}^{-1}$ and the internal heat transfer coefficient is fitted to the individual experiment. Left: column 1; right: column 2.

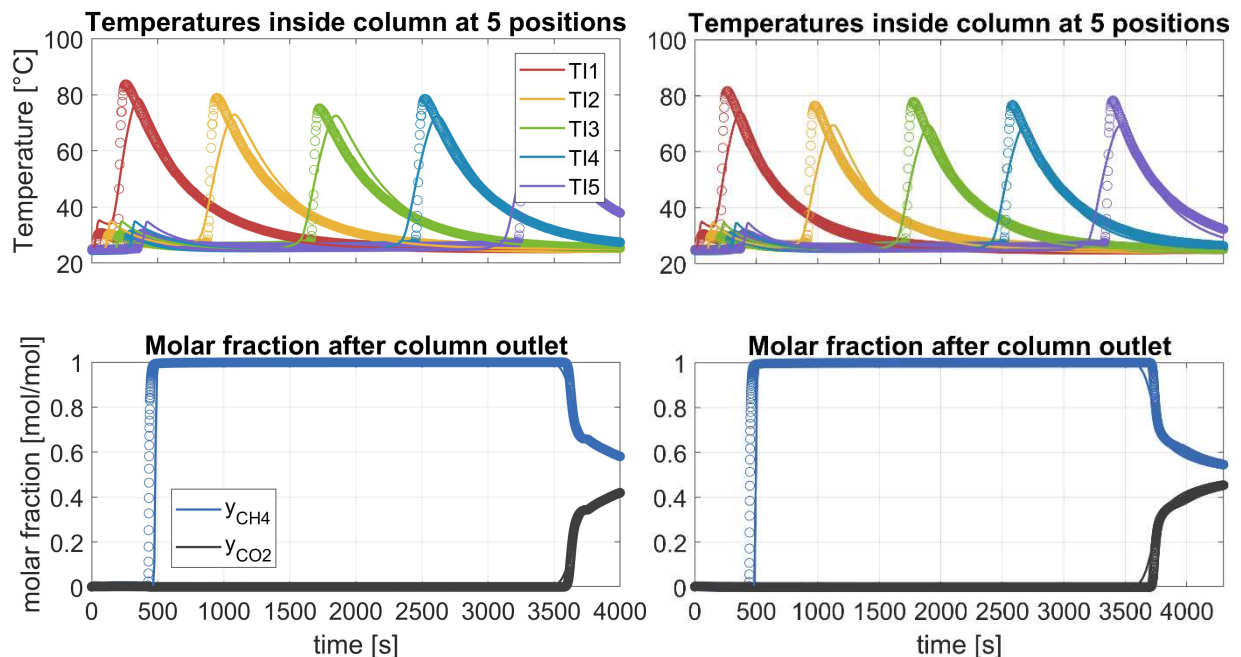


Figure 14 – Breakthrough experiments for a mixture of 50 mol% CO_2 and 50 mol% CH_4 at pressure of 1 bar, temperature of 25 °C and feed flowrate of 20 cm^3/s . The circles indicate experimental points and the lines indicate the modelling results. The linear driving force coefficients are fixed to $k_{\text{He}} = 1 \text{ s}^{-1}$, $k_{\text{CO}_2} = 0.1 \text{ s}^{-1}$ and $k_{\text{CH}_4} = 0.5 \text{ s}^{-1}$ and the internal heat transfer coefficient is fitted to the individual experiment. Left: column 1; right: column 2.

4.2.1.2 Heat transfer

In contrast to mass transfer, which was found to have little effect on the modelling results and the agreement between model and experiments for a wide range of different mass transfer coefficients, heat transfer plays a more important role. Whereas the external heat transfer influences the results, its effect is significantly less pronounced than for the internal heat transfer coefficient, and therefore a constant value of $h_w = 220 \frac{\text{W}}{\text{m}^2\text{K}}$ was chosen for all experiments in accordance with previous studies [12]. For a better prediction of each experiment, fitting it individually to each experiment is an option. The influence of the internal heat transfer coefficient h_c is significant. Therefore, it was fitted to each experiment individually whilst fixing all mass transfer coefficients.

Whereas the value chosen for the mass transfer coefficient does not influence the fitting of the heat transfer coefficient significantly (refer to the previous section), h_c can differ significantly between experiments performed in column 1 and column 2 with differences greater 4 $\text{W}/\text{m}^2\text{K}$. This is clear from Table 11, which gives the fitted internal heat transfer coefficients for all binary breakthrough experiments. This difference could have several reasons. First, the positioning of the thermocouples is not exact and only approximately at the locations indicated in Table 10 and only approximately in the center of the column. Those differences lead to differences in the measured temperatures and therefore to different optimal fits. Second, during the breakthrough experiments the thermofluid flows through both columns at the same time. Because the piping is not exactly the same, this might lead to differences in the flow pattern between both columns and therefore lead to

a higher or lower external heat transfer coefficient. However, the difference is not consistent: in some cases, the heat transfer coefficient is higher for column 1, in other cases for column 2, which makes a systematic over-/underestimation of the external heat transfer for one of the columns less likely. From Table 11, there seems to be a clear dependence of the heat transfer coefficient on pressure with increasing heat transfer coefficients for higher pressures, whereas there is no clear dependence on temperature.

Table 11 – Heat transfer coefficients for different breakthrough experiments for a mixture of 50 mol% CH₄ and 50 mol% CO₂ at different temperatures and pressures and for different columns. The internal driving force coefficients were fixed to $k_{He} = 1 \text{ s}^{-1}$, $k_{CO_2} = 0.1 \text{ s}^{-1}$ and $k_{CH_4} = 0.5 \text{ s}^{-1}$.

Column	T [°C]	P [bar]	h_c [W/m ² K]
1	25	1	19.2
2	25	1	23.5
1	25	10	26.7
2	25	10	25.2
1	25	25	31.4
2	25	25	34.2
1	45	10	23.9
2	45	10	24.3
1, repetition	45	10	23.9
2	45	25	37.8

To assess the influence of the internal heat transfer coefficient, we refitted the experiments at 25 bar and 25 °C – chosen due to the large difference in h_c – using different fixed heat transfer coefficients. Those fixed values are the average of both columns ($h_c = 32.8 \frac{\text{W}}{\text{m}^2\text{K}}$), this average $\pm 10 \%$ and this average $\pm 20 \%$. The results are shown in Figure 15 for column 2. Decreasing heat transfer coefficients are shown in the left graph and increasing heat transfer coefficients in the right graph.

The figure highlights that the effect on the temperature profiles is bigger than on the concentration profiles. For lowering the heat transfer coefficient (left figure), the temperature peaks are higher and they both increase and decrease more slowly. In addition, the breakthrough of CO₂ happens earlier due to an increased column temperature. For increasing the heat transfer coefficient (right figure), the breakthrough profiles are very similar and the difference in temperature profiles is less pronounced. The peaks are just slightly lower and the decrease is a little faster. Even a 20 % higher heat transfer still describes the experiments well. This highlights that whereas the heat

transfer coefficient plays a more important role for an accurate description of the breakthrough experiments and one fixed heat transfer coefficient cannot describe all experiments, there is a range of feasible h_c for each experiment that described the results reasonably well.

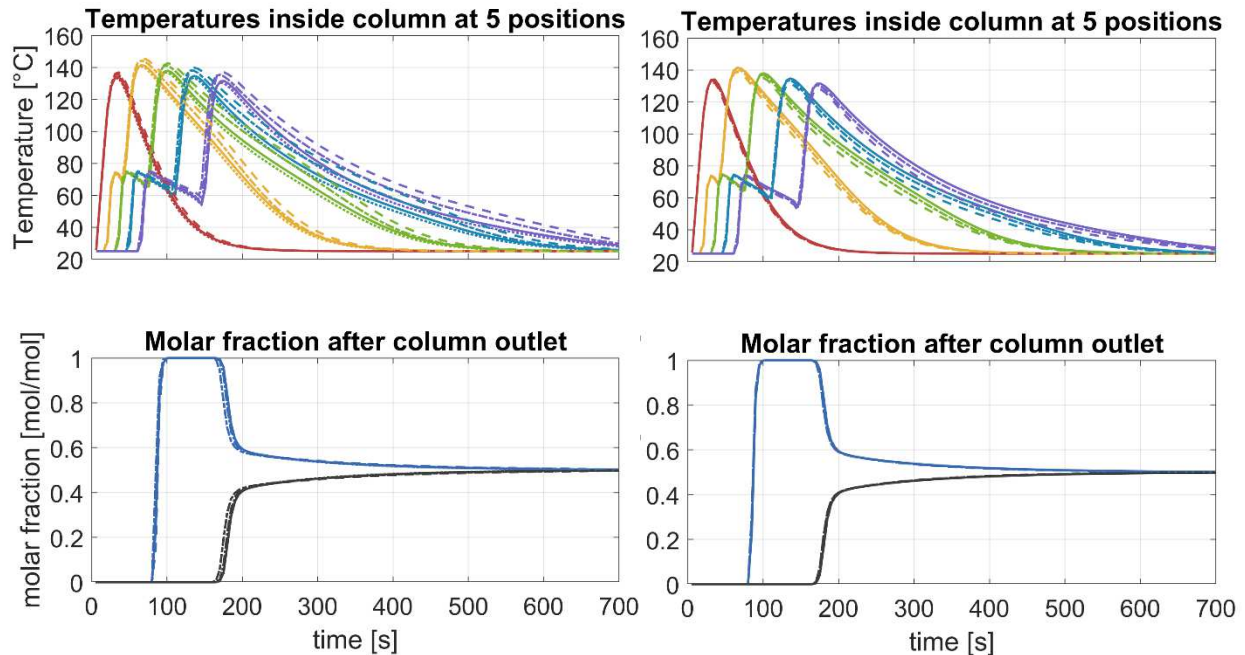


Figure 15 – Fitting of breakthrough experiment with different fixed values for the internal heat transfer coefficient. Breakthrough of a mixture of 50 mol% CO₂ and 50 mol% CH₄ at a pressure of 25 bar, a temperature of 25 °C and a feed flowrate of 20 cm³/s performed in column 2. The linear driving force coefficients are fixed to $k_{He} = 1 \text{ s}^{-1}$, $k_{CO_2} = 0.1 \text{ s}^{-1}$ and $k_{CH_4} = 0.5 \text{ s}^{-1}$. The internal heat transfer coefficient is either fitted to the experiment or fixed. Solid lines indicate the case where h_c is fitted resulting in $h_c = 34.2 \frac{W}{m^2K}$, dotted lines indicate the case where the average of the fitted h_c for column 1 and column 2 is used ($h_c = 32.8 \frac{W}{m^2K}$), dash-dotted lines are for a case 10 % lower (left) or higher (right) than this average and dashed lines for a case 20 % lower (left) or higher (right) than this case.

4.2.2 Ternary breakthrough experiments

The ternary breakthrough experiments were performed for a mixture of 20 mol% CO₂, 75 mol% H₂ and 5 mol% CH₄ for different flowrates and pressures. A typical breakthrough experiment is shown in Figure 16 for a pressure of 10 bar, a temperature of 25 °C and a feed flowrate of 20 cm³/s. For modelling the experiment, fixed transport parameters $k_{He} = 1 \text{ s}^{-1}$, $k_{CO_2} = 0.1 \text{ s}^{-1}$, $k_{H_2} = 1 \text{ s}^{-1}$ and $k_{CH_4} = 0.5 \text{ s}^{-1}$ were used. The temperatures inside the column at five different locations are shown at the top of the figure and the composition measured after the column at the bottom of the figure. Circles indicate the measured points and lines the modelling results for the same experiment whilst fitting the feed velocity (to account for errors of the MFCs) and the internal heat transfer coefficient. The bottom part shows the breakthrough of the three different components at three different times. H₂ adsorbs little and breaks through first. Due to the low adsorption, only a very slight increase in temperature can be observed as the H₂ front propagates through

the column. Methane features a stronger adsorption capacity than H₂ and breaks through second. A temperature front related to methane adsorption propagates through the column with temperatures increasing approximately 15 K. The increase is lower than for the binary experiments due to the lower concentration of methane. CO₂ adsorbs the strongest and breaks through last. A front of high temperatures propagates through the column reaching temperatures up to 130 °C.

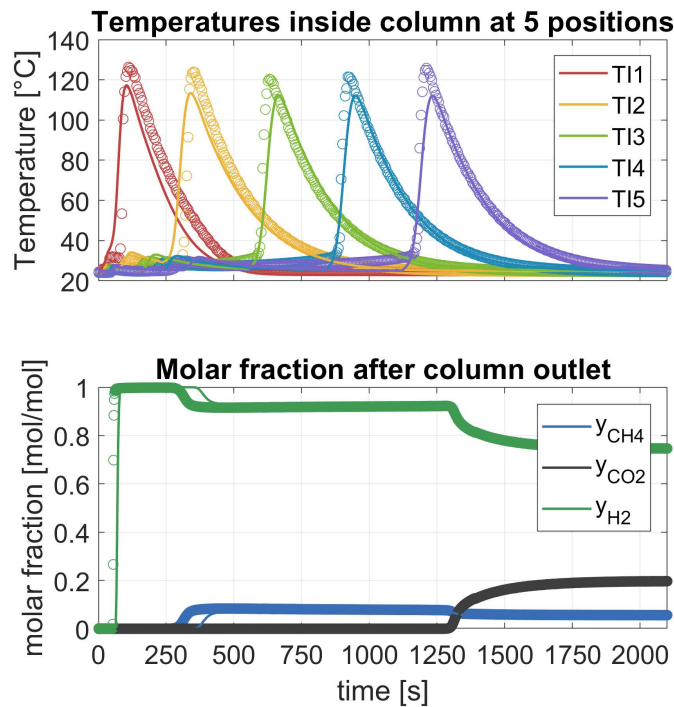


Figure 16 – Breakthrough experiment for a mixture of 20 mol% CO₂, 75 mol% H₂ and 5 mol% CH₄ at a pressure of 10 bar, a temperature of 25 °C and a feed flowrate of 20 cm³/s. The circles indicate experimental points and the lines indicate the modelling results. The linear driving force coefficients are fixed to $k_{He} = 1 \text{ s}^{-1}$, $k_{CO_2} = 0.1 \text{ s}^{-1}$, $k_{H_2} = 1 \text{ s}^{-1}$ and $k_{CH_4} = 0.5 \text{ s}^{-1}$. The internal heat transfer coefficient $h_c = 34.6 \frac{W}{m^2K}$ is fitted to the individual experiment.

Whereas both the H₂ and CO₂ breakthrough can be predicted nicely, it is evident that the methane breaks through earlier than predicted by the model, which emphasizes the difficulty in modelling multicomponent adsorption. Also for the other breakthrough experiments at different pressures and velocities, the fits are worse than for the binary mixtures, as shown in Figure 17. In both cases, H₂ and CH₄ breakthrough are predicted later than they occur experimentally.

As for the binary breakthrough experiments, also for the ternary breakthrough experiments, there is a low sensitivity when changing the mass transfer coefficients within a certain range and the same fixed values as before can be used. For H₂ (similar to He), mass transfer is fast and a value of $k_{H_2} = 1 \text{ s}^{-1}$ performs well for fitting all experiments. The mass transfer coefficients suggested are summarized in Table 12.

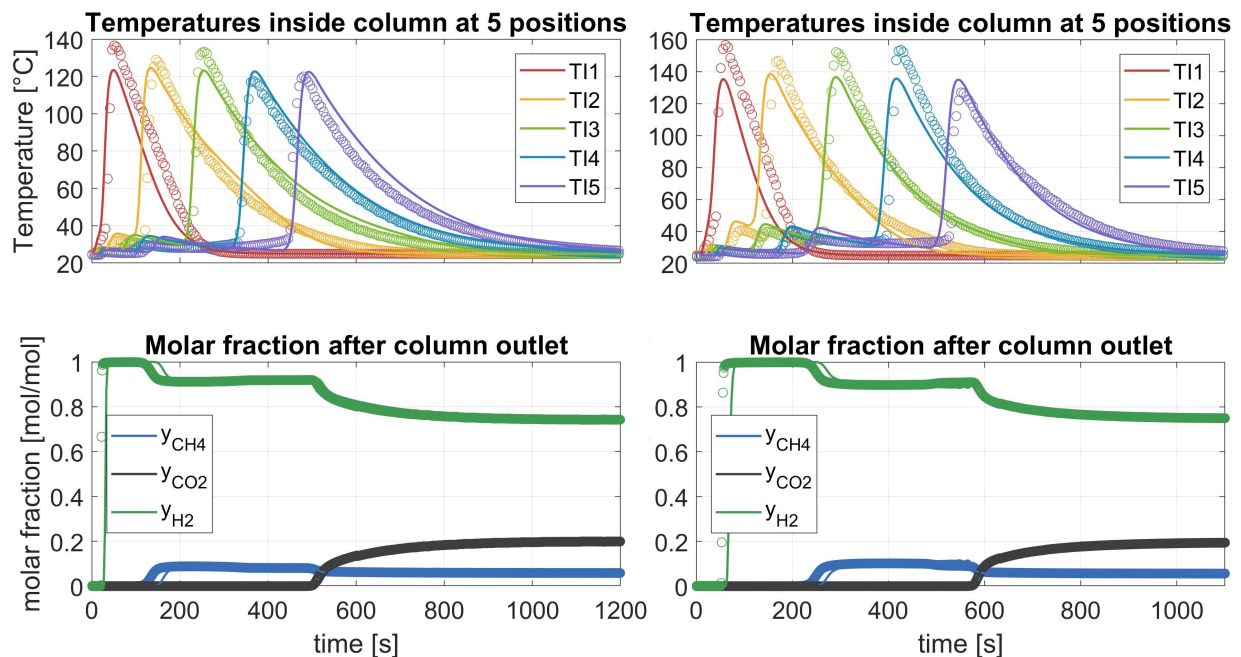


Figure 17 – Breakthrough experiment for a mixture of 20 mol% CO₂, 75 mol% H₂ and 5 mol% CH₄. Left: pressure of 10 bar, temperature of 25 °C, feed flowrate of 40 cm³/s. Right: pressure of 25 bar, temperature of 25 °C, feed flowrate of 20 cm³/s. The circles indicate experimental points and the lines indicate the modelling results. The linear driving force coefficients are fixed to $k_{He} = 1 \text{ s}^{-1}$, $k_{CO_2} = 0.1 \text{ s}^{-1}$, $k_{H_2} = 1 \text{ s}^{-1}$ and $k_{CH_4} = 0.5 \text{ s}^{-1}$. The internal heat transfer coefficient is fitted to the individual experiment with $h_c = 32.0 \frac{W}{m^2K}$ (left) and $h_c = 39.0 \frac{W}{m^2K}$ (right).

Table 12 – Average fitted mass transfer coefficients on zeolite 13X.

$k_{H_2} [\text{s}^{-1}]$	$k_{He} [\text{s}^{-1}]$	$k_{CO_2} [\text{s}^{-1}]$	$k_{CH_4} [\text{s}^{-1}]$
1	1	0.1	0.5

4.3 Zeolite CaX

Zeolite CaX was examined mainly due to its relatively strong N₂ adsorption. Nitrogen is present in small but significant amounts in SMR syngas (compare Table 7) and is often the leading impurity front due to its weak adsorption and low concentration in the feed. Enhancing N₂ adsorption and thereby prolonging the breakthrough of N₂ is essential to reach high H₂ purities: longer adsorption times are possible without N₂ breaking through and contaminating the H₂ product. Adding zeolite CaX to an adsorbent that features a low N₂ adsorption, but is otherwise very promising for the CO₂-H₂-impurity separation could enhance the overall process performance and/or enable the production of H₂ at the required purity.

4.3.1 Adsorption isotherms

The measured adsorption isotherms of CH₄, CO₂, CO and N₂ on zeolite CaX together with fitted DSL isotherms for the three different temperatures and fitted temperature

dependent Sips isotherms (dotted lines) are shown in Figure 18. The corresponding isotherm parameters for the DSL fits are reported in Table 13 and for the temperature dependent Sips isotherms in Table 14. For CO_2 , in addition to three isotherms measured with the volumetric setup for pressures up to 1 bar (shown as empty symbols in Figure 18), an isotherm has been measured on the gravimetric setup for 25 °C and up to 30 bar (shown with filled circles). It is also shown for higher pressures in Figure 19.

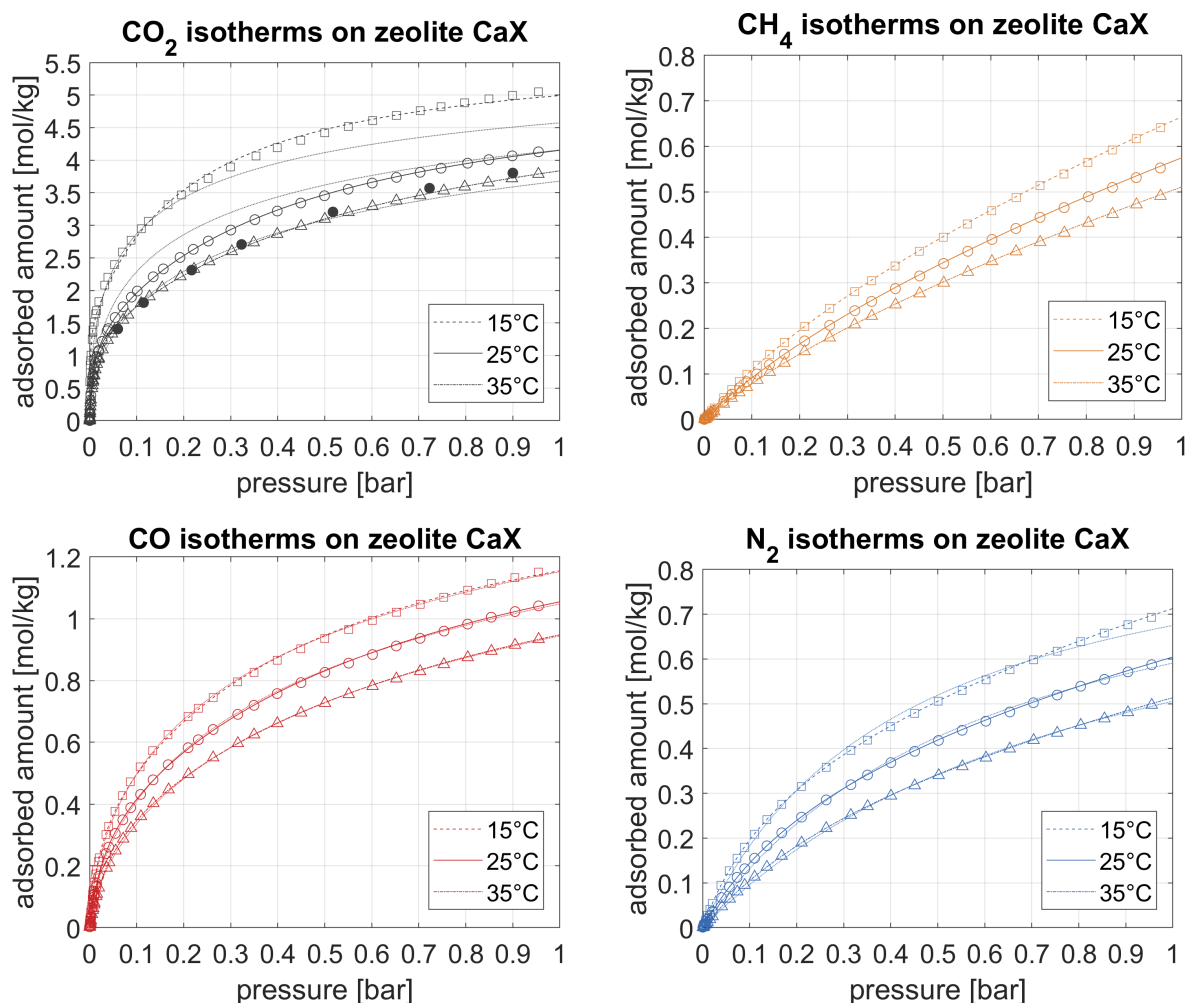


Figure 18 – Measured isotherms on zeolite CaX at 15 °C (squares), 25 °C (circles) and 35 °C (triangles) for different gases (CO_2 , CH_4 , CO and N_2). The fitted DSL isotherms for the different temperatures are shown as lines with the isotherm parameters being reported in Table 13. The temperature dependent Sips isotherms are shown as dotted lines with the respective isotherm parameters being reported in Table 14. For CO_2 , the filled circles indicate an isotherm measured at 25 °C on the gravimetric setup up to 30 bar (refer also to Figure 19), whereas all other points were measured on the volumetric setup up to 1 bar only.

It is important to mention that a temperature dependent DSL model fits the experimental data well for all components. However, to apply the DSL formulation correctly, the energetic site matching issue needs to be considered [20]. The DSL model assumes two adsorption sites with different energies. The site matching issue thus refers to the fact that in a multicomponent system, the components might not all see site one as high-free-

energy site. In a binary system, there would be two different pairings: perfect positive when both adsorbates see site one as high-free-energy site and perfect negative when each adsorbate sees a different site as high-free-energy site.

Table 13 – DSL parameters for CO₂, CH₄, CO and N₂ on zeolite CaX for 15, 25 and 35 °C.

	unit	T	CO ₂	CH ₄	CO	N ₂
a_i^{inf}	[mol/kg]	288	1.4600	0.18000	0.34000	0.37862
b_i	[1/ bar]	288	916.50	3.5331	56.578	6.3642
c_i^{inf}	[mol/kg]	288	4.2757	3.1177	1.2265	1.6839
d_i	[1/ bar]	288	4.7680	0.20241	2.0253	0.29696
a_i^{inf}	[mol/kg]	298	1.2780	0.18239	0.34193	0.40599
b_i	[1/ bar]	298	133.97	2.8695	34.476	3.7872
c_i^{inf}	[mol/kg]	298	4.1415	3.1000	1.2512	1.8544
d_i	[1/ bar]	298	2.2923	0.16538	1.3664	0.18028
a_i^{inf}	[mol/kg]	308	1.3500	0.17347	0.32000	0.37428
b_i	[1/ bar]	308	92.709	2.5992	24.268	2.6356
c_i^{inf}	[mol/kg]	308	4.2294	3.6048	1.2365	2.1568
d_i	[1/ bar]	308	1.4472	0.11981	1.0755	0.12657

Table 14 – Isotherm parameters for CO₂, CH₄, CO and N₂ on zeolite CaX fitted to a temperature dependent Sips isotherm equation.

	unit	CO ₂	CO	N ₂	CH ₄
$A_{1,i}$	[mol/kg]	6.1081	1.9343	0.96354	10.078
$A_{2,i}$	[mol/kg/K]	0	0	0	0
$B_{0,i} \times 10^5$	[1/ bar]	0.000791	4.6565	2.2337	61.623
$B_{1,i}$	[K]	5968.0	3049.9	3328.9	1180.9
$C_{1,i}$	[-]	-0.44508	0.53872	1	0.84646
$C_{2,i}$	[K]	673.78	302.66	0	114.18

The number of viable combinations increases to four in a system with three components and continues to increase with the number of adsorbates [21]. To confirm perfect positive or perfect negative behavior, binary adsorption equilibria are necessary, which were not available for zeolite CaX. We therefore decided against using a DSL model, even though it can predict the experimental data better, because its application in process modelling without addressing the energetic site matching issue can result in very different outcomes.

Figure 18 also shows that zeolite CaX indeed features a strong nitrogen adsorption with a slope steeper than for CH₄ and a similar capacity as CH₄ at 1 bar. This emphasizes that the material indeed has promise for enhancing N₂ adsorption.

In addition to the datapoints shown in Figure 18, another high-pressure CO₂ isotherms was measured on the gravimetric setup at 65 °C to assess if a temperature dependence fitted to low-pressure data only (up to 1 bar) can be extrapolated to predict also the high-pressure data at different temperatures with a sufficient accuracy.

Both high-pressure isotherms are shown in Figure 19. The figure shows that also at high pressures, the Sips isotherm for 25 °C does not fit the data particularly well. However, the prediction of the CO₂ adsorption at 65 °C is rather satisfactory given that we extrapolate both for temperature and for pressure.

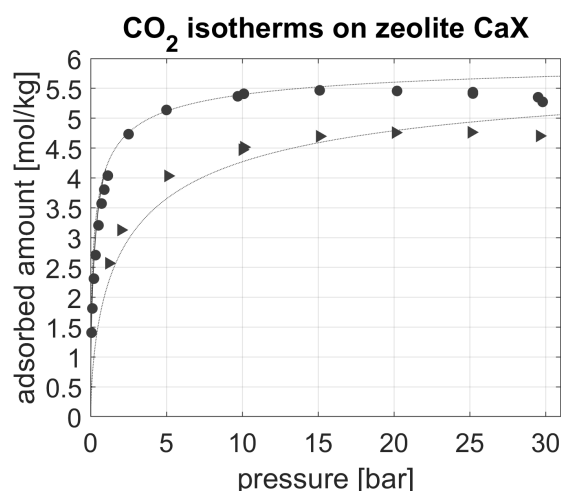


Figure 19 – Measured CO₂ isotherms on zeolite CaX at 25 °C (filled circles) and 65 °C (filled triangles). The dotted lines give the fit with a temperature dependent Sips isotherm equation using the data at 25 °C as well as low-pressure CO₂ adsorption data shown in Figure 18. The measured data at 65 °C was not used for fitting the isotherm equation, but only for testing the predictive capability of the isotherm fit extrapolated to higher temperatures and pressures.

4.3.2 Isosteric heat of adsorption

The heats of adsorption averaged over all three temperatures are shown in Figure 20. Whereas the heat of adsorption is very high for CO₂, especially at high loadings with almost 90 kJ/mol, it is similar for both CO and N₂ in the range of 30 kJ/mol and much lower for CH₄ (around 13 kJ/mol). The heat of adsorption for CO₂ is much higher than

e.g. for zeolite 13X. As shown in section 3.4, this has a strong influence on the separation performance and makes the material less favorable for CO₂-H₂-impurity separation.

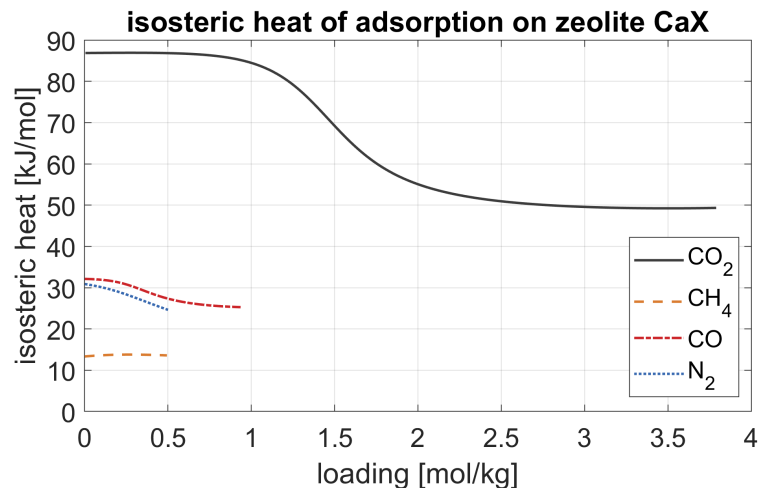


Figure 20 – Isosteric heat of adsorption for CO₂, CH₄, CO and N₂ on zeolite CaX for different loadings averaged over temperature (15, 25 and 35 °C). Only the loadings up to which measurements for all three temperatures were available were considered for the evaluation.

4.4 Activated Carbon

An activated carbon has been examined when developing the VPSA cycles based on literature adsorption isotherms [22]. It has been shown that the separation performance is worse than for zeolite 13X due to the strong methane adsorption and the low selectivity of CO₂ over methane, which makes it difficult to reach the desired CO₂ separation performance with 96 % purity at 90 % recovery [3]. However, AC could be of interest as first layer in a layered bed to adsorb the bulk of the CO₂ impurity, or for applications with wet streams because of its reversible water adsorption at low relative humidity [23]. We therefore completed the characterization of activated carbon measuring isotherms for CH₄ and Ar in addition to the previously measured isotherms for CO₂, N₂, H₂ and H₂O [23] [5].

4.4.1 Adsorption isotherms

The measured adsorption isotherms for CH₄ and Ar on AC together with the fitted temperature dependent Sips isotherm equation are shown in Figure 21. The corresponding isotherm parameters are reported in Table 15.

The affinity of CH₄ on AC is higher than that of Ar. Both isotherms flatten below 30 bar, but are not approximating their maximum capacity yet. Especially for Ar, the maximum capacity seems to be reached at significantly higher pressures. It is interesting to note that the fitted maximum capacity for both is very similar (just above 7 mol/kg) with a higher affinity coefficient for CH₄ – 0.48 1/MPa for CH₄ at 35 °C in comparison to 0.18 1/MPa for Ar – as shown in Table 15. The Sips isotherm equation fits the experimental data very well without having to add a temperature dependence for the maximum capacity.

A comparison with other materials showing also the CO₂ and N₂ adsorption will follow in section 6.

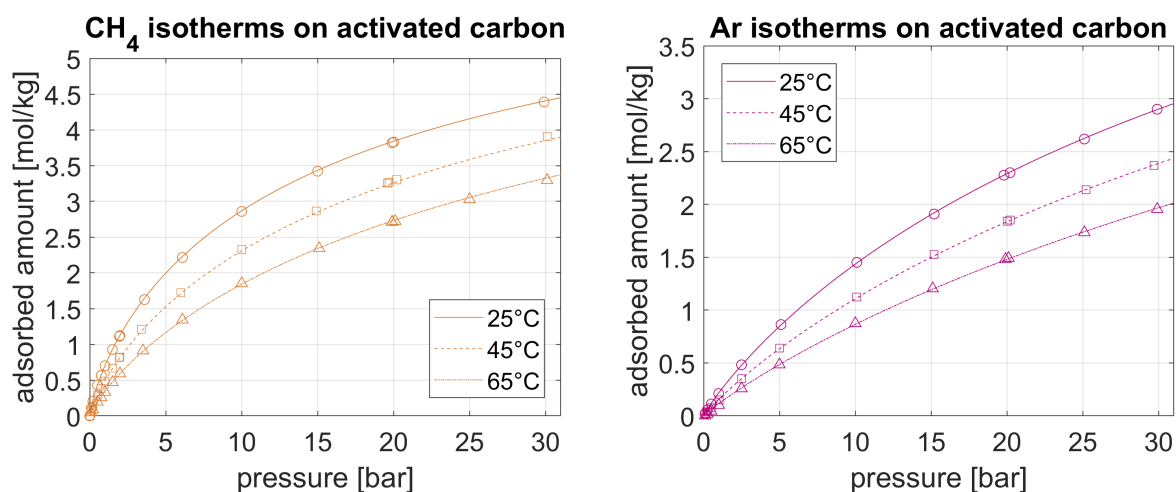


Figure 21 – Measured isotherms on activated carbon at 25 °C (circles), 45 °C (squares) and 65 °C (triangles) for different gases (CH₄ and Ar). The fitted temperature dependent Sips isotherms are shown as lines with the respective isotherm parameters being summarized in Table 15.

Table 15 – Sips parameters for CH₄ and Ar on activated carbon. For the sake of completeness, also the isotherm parameters for H₂, CO₂ and N₂ from previous measurements [5] are included.

	unit	CH ₄	Ar	H ₂	CO ₂	N ₂
T_{ref}	[K]	298.15	298.15	273	329	273
$\alpha_{1,i}$	[mol/kg]	7.2240	7.3457	16.66	1.38	2.82
$\alpha_{2,i}$	[mol/kg/K]	0	0	0	-5628	-1706
$\beta_{0,i}$	[MPa ⁻¹]	9.5275e-4	1.0904e-3	6.97e-4	1.68e-2	1.74e-3
$\beta_{1,i}$	[J/mol]	-15928	-13013	-9826	-9159	-12661
$\gamma_{1,i}$	[-]	-0.71694	96.390	0	0.072	0
$\gamma_{2,i}$	[1/K]	-1.5404e-3	4.6017e-6	0	0.106	0
$\gamma_{3,i}$	[-]	0.78683	0.90034	0.96	0.83	0.86

4.4.2 Isosteric heat of adsorption

The heats of adsorption averaged over all three temperatures are shown in Figure 22. Whereas CH₄ features a higher heat of adsorption for low loadings (25 kJ/mol), which translates to a higher affinity at those loadings, it approximates the same values as Ar for higher loadings (14 kJ/mol). The heat of adsorption for CH₄ is approximately half that of CH₄ on zeolite 13X and higher than on zeolite CaX, whereas for Ar it is in the same range as for zeolite 13X.

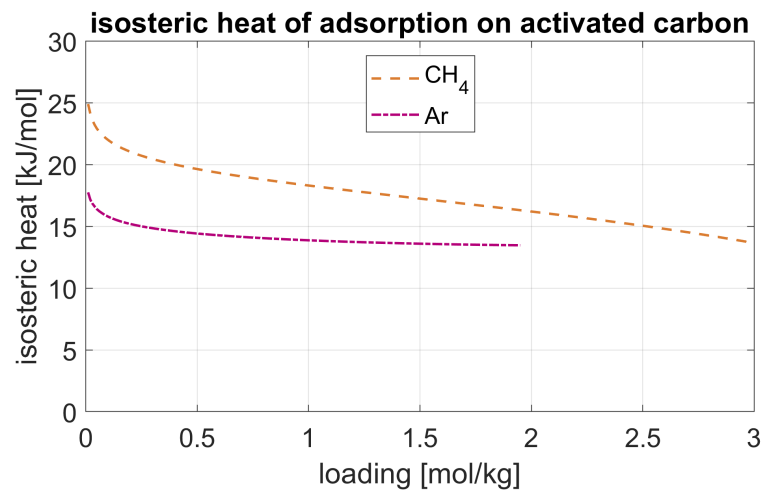


Figure 22 – Isosteric heat of adsorption for CH₄ and Ar on activated carbon for different loadings averaged over temperature (25, 45 and 65 °C). Only the loadings up to which measurements for all three temperatures were available were considered for the evaluation.

5 NOVEL ADSORBENTS

Metal organic frameworks (MOFs) have emerged as adsorbent candidates for different applications. MOFs are metal complexes bonded with organic ligands that can form various morphologies as porous materials. They are characterized by tailorable pore size, high surface area, tunable chemical functionalities and good thermal and mechanical stabilities [24] [25]. In the context of CCS, MOFs have been designed and tested for the separation of CO₂ from different components like N₂ and H₂ and several reviews exist on CO₂ separation using MOFs as adsorbents [24] [26] [27].

For a standard CO₂ capture application, a high selectivity of CO₂ over other components is essential [28]. For the VPSA process, however, also the impurities like N₂, CH₄, CO and Ar should have a significant uptake on the adsorbent material to reach high H₂ purities. Therefore, many of the MOFs commonly suggested for CO₂ capture applications are not suitable for VPSA for H₂-CO₂-impurity separation like UTSA16 [29] due to its very high selectivity of CO₂ over N₂. Many other MOFs are unstable under moist conditions like HKUST-1 (Cu-BTC) [30]. An extensive literature review was carried out and a collaboration between material scientists at EPFL and process modelers at ETHZ has been established to find the most promising material for this application. Cu-TDPAT, an rht-type dual-functionalized MOF, was identified as most promising material for further characterization.

5.1 Cu-TDPAT

Cu-TDPAT and other rht-MOFs have been studied in literature with Cu-TDPAT showing the highest selectivity and capacity for CO₂ [31]. Due to its large pore volumes it is expected to become increasingly attractive with higher pressures compared to the commonly used zeolites with lower pore volumes. It therefore has significant potential for use as adsorbent for high-pressure gas separation and has been suggested for H₂ and natural gas purification [32].

5.1.1 Adsorption isotherms

The measured adsorption isotherms of CO₂, CH₄, CO and N₂ on Cu-TDPAT are shown in Figure 23 together with fitted DSL isotherms for the three different temperatures and fitted temperature dependent Sips isotherms. The corresponding isotherm parameters are reported in in Table 16 for the DSL fits and in Table 17 for the Sips fits. In addition to the low-pressure data, data at high pressure was measured for both CO₂ and H₂ at 25 °C, which is shown in Figure 24

Looking at the low-pressure data only (Figure 23), it is clear that the material features a strong CO₂ adsorption and a strong affinity towards CO. The isotherms for both components are steep in the origin and level off slightly up to 1 bar, but are still far from reaching the maximum capacity. For CO₂, the capacity at 30 bar (shown in Figure 24) is around 4 times the capacity at 1 bar and the very flat slope of the isotherm suggests that at 30 bar, Cu-TDPAT is close to reaching its maximum CO₂ capacity.

For CH₄ and N₂, the isotherms are linear up to 1 bar. The capacity at 1 bar is very low for N₂ – approximately 0.25 mol/kg, whereas for CH₄, the uptake at 1 bar is similar to the CO uptake at the same pressure and about four times that of N₂. Having isotherm data only in the linear region for CH₄ and N₂ makes it difficult to fit the maximum capacity because

it is not well defined. However, the isotherms for CO, CH₄ and N₂ are fitted well with both temperature independent DSL isotherms and temperature dependent Sips isotherms. For CO₂, the DSL fits are better, whereas the Sips isotherm equation underestimates the adsorption in the low-pressure range and overestimates it above 0.5 bar. Similar to zeolite CaX, energetic site matching adds large uncertainty when modelling processes with mixtures of several gases (in this case up to five components for SMR and up to six components for ATR) with a DSL isotherm. Therefore, we did not fit temperature dependent DSL isotherms.

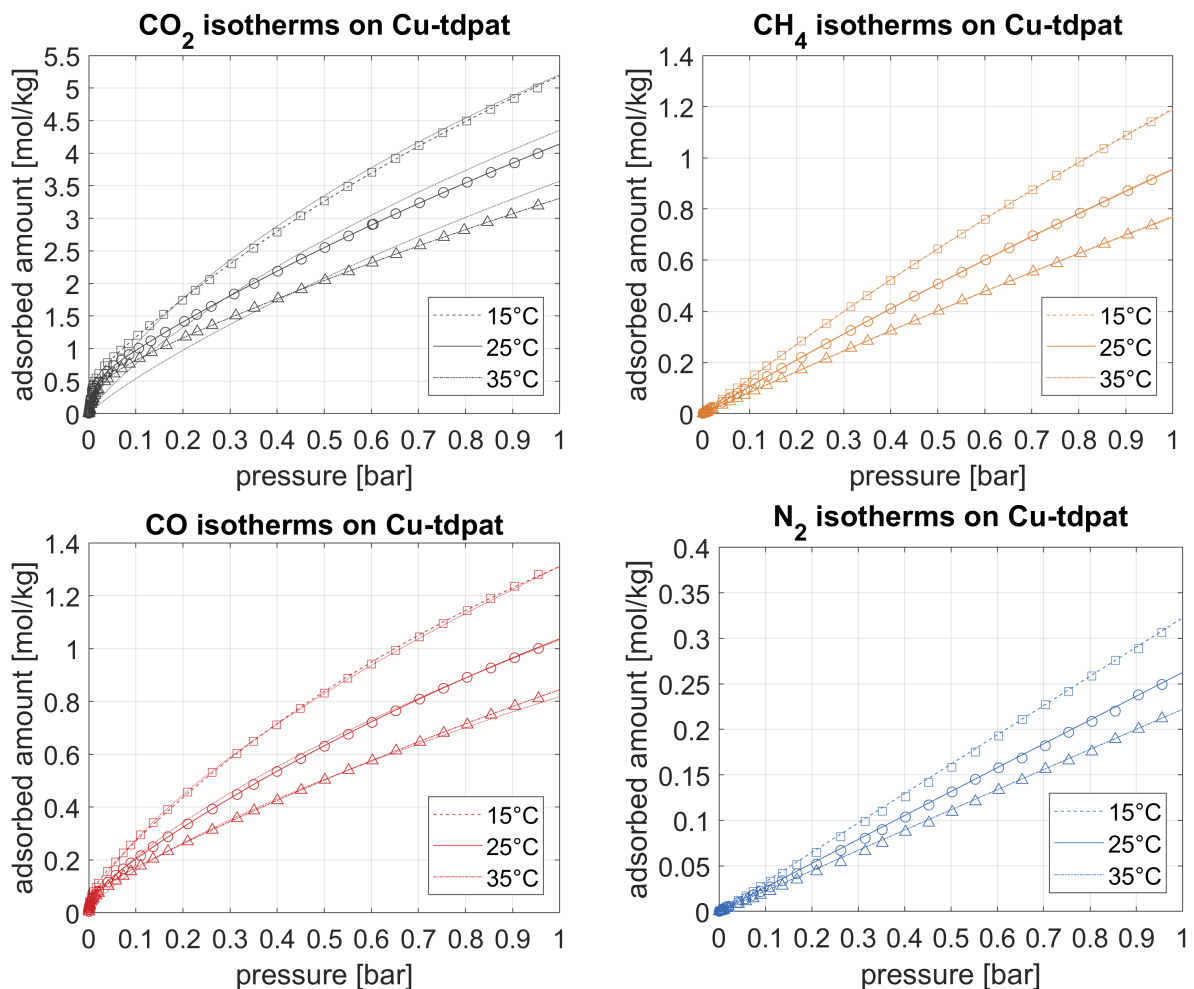


Figure 23 – Measured isotherms on Cu-TDPAT at 15 °C (squares), 25 °C (circles) and 35 °C (triangles) for different gases (CO₂, CH₄, CO and N₂). The fitted DSL isotherms for the different temperatures are shown as lines with the isotherm parameters reported in Table 16. The temperature dependent Sips isotherms are shown as dotted lines with the respective isotherm parameters being reported in Table 17.

The H₂ isotherm shown in Figure 24 features a long linear region up to approximately 40 bar and then starts decreasing slightly in slope. However, even at 180 bar, it is still far from reaching its maximum capacity. The uptake is significantly lower than for any other component and in the range of 0.03 mol/kg at 1 bar partial pressure. The H₂ adsorption at feed stream composition and pressure as reported in Table 7 (H₂ partial pressure of 19 bar) is significantly higher in the range of 0.6 mol/kg.

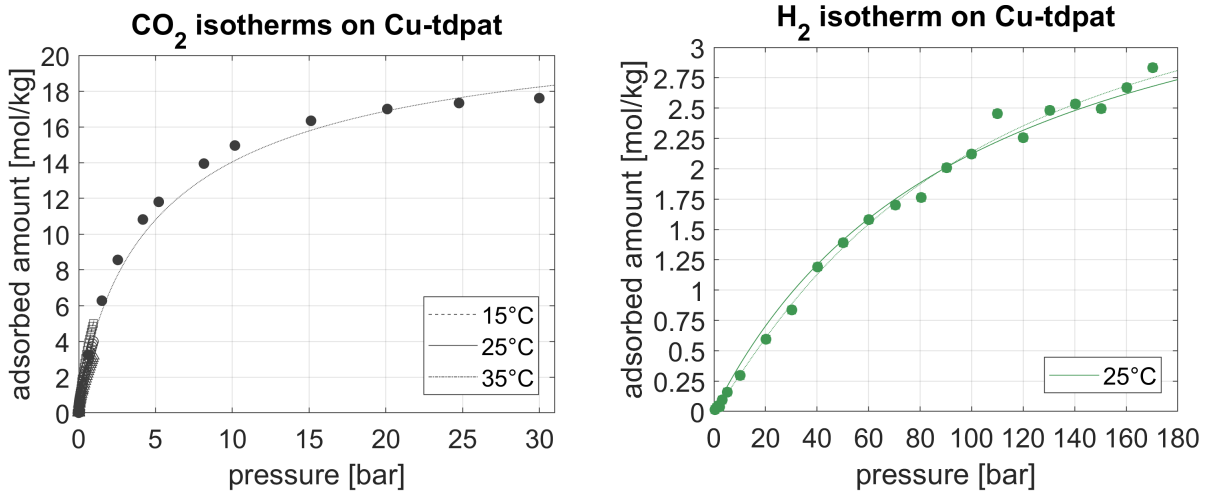


Figure 24 – Measured high-pressure isotherms of CO₂ and H₂ on Cu-TDPAT at 25 °C (filled circles). For CO₂, also the low-pressure isotherms up to 1 bar are shown as empty symbols for 15 °C (squares), 25 °C (circles) and 35 °C (triangles). The fitted DSL isotherms are shown as lines as indicated in the legend and the Sips fits as dotted lines.

Table 16 – DSL parameters for CO₂, CH₄, CO and N₂ on Cu-TDPAT for 15, 25 and 35 °C and for H₂ at 25 °C.

	unit	T	CH ₄	CO	CO ₂	N ₂	H ₂
a_i^{inf}	[mol/kg]	288	1.6092e-6	0.09412	0.58571	0.010093	-
b_i	[1/ bar]	288	0.26144	265.41	203.28	0.42232	-
c_i^{inf}	[mol/kg]	288	7.9106	3.3374	16.290	256.27	-
d_i	[1/ bar]	288	0.17739	0.57378	0.39410	0.0012491	-
a_i^{inf}	[mol/kg]	298	1.5244e-5	0.09	0.59574	0.010001	3.8732e-4
b_i	[1/ bar]	298	0.12943	85.027	99.979	0.28974	5.7479
c_i^{inf}	[mol/kg]	298	8.3350	3.6825	18.347	173.42	4.2796
d_i	[1/ bar]	298	0.12962	0.34681	0.24002	0.0015044	9.8317e-3
a_i^{inf}	[mol/kg]	308	3.7731e-6	0.09	0.59543	0.011814	-
b_i	[1/ bar]	308	0.0094913	99.152	55.209	0.038121	-
c_i^{inf}	[mol/kg]	308	9.3331	4.3021	18.398	29.028	-
d_i	[1/ bar]	308	0.090035	0.21295	0.17364	0.0076989	-

Table 17 – Isotherm parameters for CO₂, CH₄, CO, N₂ and H₂ on Cu-TDPAT fitted to a temperature dependent Sips isotherm equation.

	unit	CO ₂	CO	H ₂	N ₂	CH ₄
$A_{1,i}$	[mol/kg]	22.790	18.2	4.2224	6.7609	7.5203
$A_{2,i}$	[mol/kg/K]	0	0	0	0	0
$B_{0,i} \times 10^5$	[1/ bar]	106.50	0.35041	1022.0	24.069	11.284
$B_{1,i}$	[K]	1522.8	2566.7	0	1576.8	2137.9
$C_{1,i}$	[-]	-1.0361	0.74847	0.88626	0.90004	0.87302
$C_{2,i}$	[K]	666.77	195.58	0	14.820	35.384

5.1.2 Isostatic heat of adsorption

The heats of adsorption averaged over all three temperatures are shown in Figure 25. Even though the CO₂ uptake is very high, the heat of adsorption is only about half that of CO₂ on zeolite CaX and reaches a low value of 25 kJ/mol at high CO₂ loadings, which is expected to be favorable for the separation performance of H₂-CO₂-impurity separation, as explained before. Also for N₂, the heat of adsorption on Cu-TDPAT is only about half that of adsorption on zeolite CaX, which features a strong N₂ adsorption. For CO and CH₄, the heat of adsorption on Cu-TDPAT is slightly higher than on CaX. The average heat of adsorption for CH₄ on Cu-TDPAT is similar to CH₄ adsorption on AC and just above the lower boundary for CH₄ adsorption on zeolite 13X. In contrast to those, however, it does not decrease significantly for higher loadings.

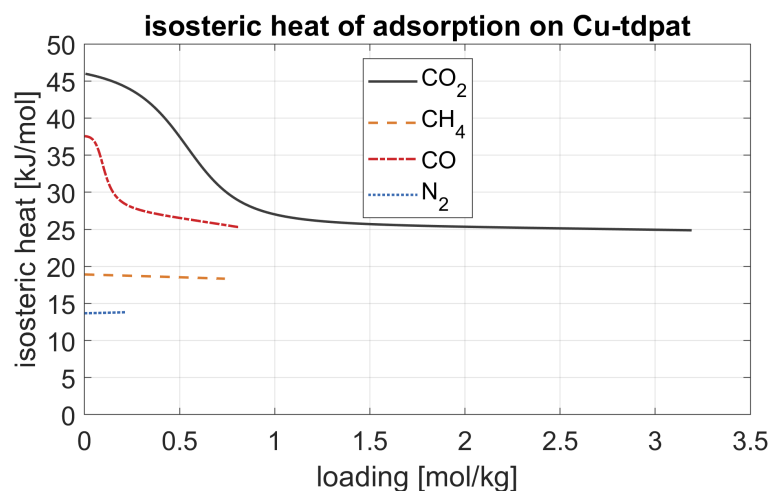


Figure 25 – Isostatic heat of adsorption for CO₂, CH₄, CO and N₂ on Cu-TDPAT for different loadings averaged over temperature (15, 25 and 35 °C). Only the loadings up to which measurements for all three temperatures were available were considered for the evaluation.

6 COMPARISON OF DIFFERENT ADSORBENTS

This chapter focusses on a comparison between the different adsorbents based on the adsorption isotherms and simple adsorption metrics like the cyclic CO₂ capacity. The discussion will also touch on implications for the cycle when choosing one or the other adsorbent. The isotherms for all four materials and up to five components are shown in Figure 26 for both the low-pressure range (left) and the high-pressure range (right) at a temperature of 25 °C. The isotherms are calculated using the parameters for the temperature dependent Sips equation as reported before for all materials.

6.1 CO₂ adsorption and cyclic capacity

Both zeolites feature a strong affinity for CO₂ with the slope and the maximum capacity being higher for zeolite 13X. Activated Carbon reaches a maximum capacity that is higher than for zeolite 13X and zeolite CaX, but the affinity is very low and the adsorption at e.g. 1 bar significantly lower than for both zeolites with just above 1.5 mol/kg adsorbed compared to over 4 mol/kg for zeolite CaX and over 5 mol/kg for zeolite 13X. For Cu-TDPAT, the affinity is lower than for both zeolites, but the maximum capacity is in the range of four times that of the zeolites, which potentially compensates for the lower affinity. At 1 bar, the uptake is close to the uptake of both zeolites with just below 4.5 mol/kg. To understand the process implications of the different CO₂ isotherms better, the cyclic capacity for 25 °C is reported in Table 18 for four cases:

- For a HP with pure CO₂ at 1 bar and an evacuation at 0.1 bar
- For a HP with pure CO₂ at 1 bar and an evacuation at 0.2 bar
- For adsorption at the feed CO₂ partial pressure (4 bar, see Table 7) until the column is saturated in CO₂ and desorption at 0.1 bar
- For a HP with pure CO₂ at 1 bar and complete regeneration through evacuation and a subsequent purge under vacuum (LP) with H₂ product. Even though this purge is included in the cycle (see Figure 2 and refer to D1.1.1 [3]), the purge duration is limited and this case therefore presents a utopia scenario. The cyclic capacity reduces to the adsorbed amount at 1 bar.

Table 18 – Cyclic CO₂ capacity at 25 °C for a) HP with pure CO₂ at 1 bar and evacuation at 0.1 bar; b) HP with pure CO₂ at 1 bar and evacuation at 0.2 bar; c) adsorption until the column is saturated at 4 bar (feedstream partial pressure) and evacuation at 0.1 bar and d) utopia case with complete regeneration: HP with pure CO₂ at 1 bar followed by complete regeneration.

	unit	Zeolite 13X	Zeolite CaX	AC	Cu-TDPAT
Case a)	[mol/kg]	1.6	1.9	1.3	3.6
Case b)	[mol/kg]	1.1	1.3	1.1	3.0
Case c)	[mol/kg]	2.4	2.7	3.4	9.0
Case d)	[mol/kg]	5.3	4.2	1.6	4.3

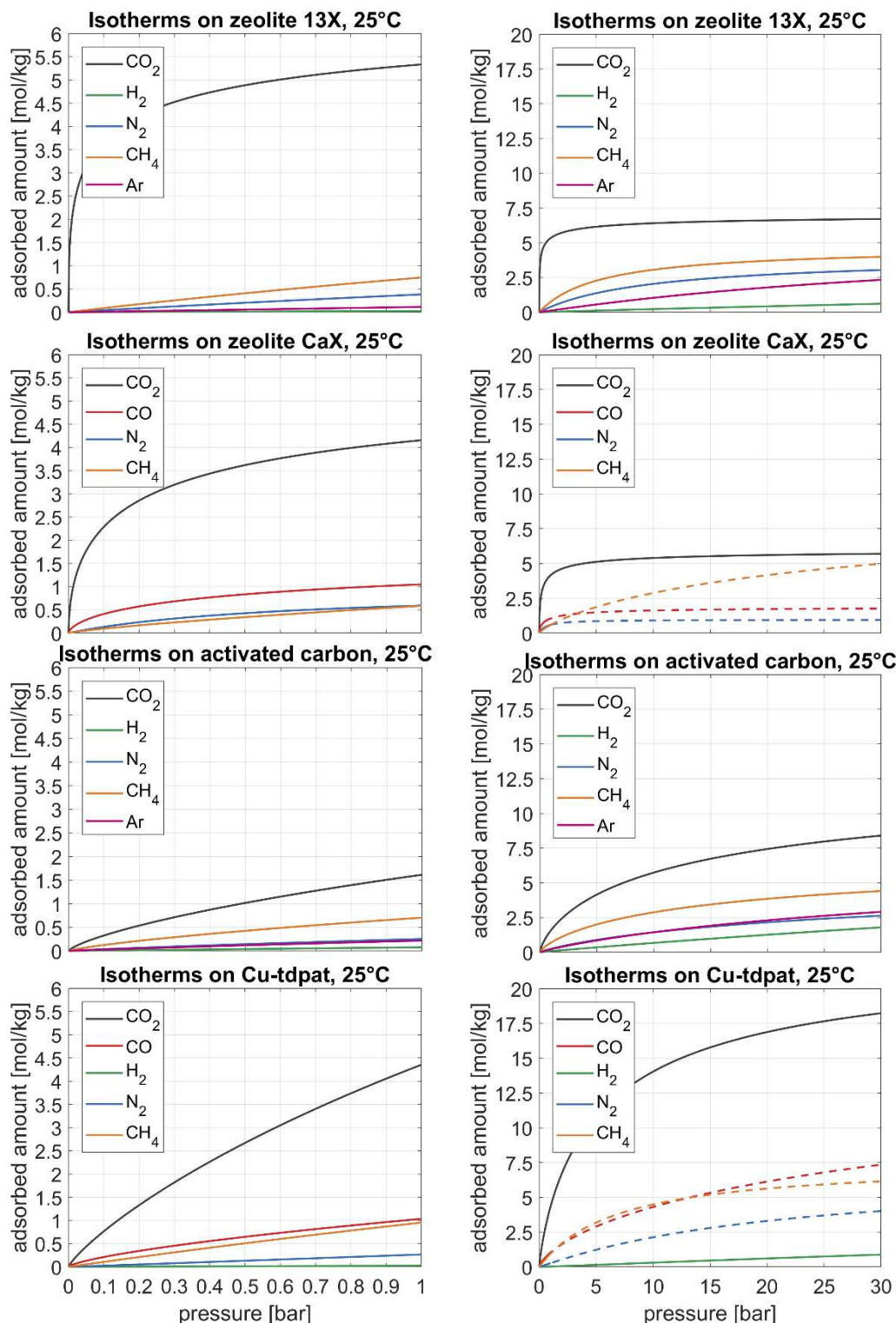


Figure 26 – Adsorption isotherms for zeolite 13X, zeolite CaX, activated carbon and MOF Cu-TDPAT calculated with the temperature dependent Sips isotherm. On the left, the isotherms are shown up to pressures of 30 bar. Not all isotherms were measured up to those pressures on all materials. Extrapolated data therefore is represented as dashed lines whereas data that has been fitted to measurements up to that pressure range is shown as solid lines.

The table shows that except for case d), Cu-TDPAT features the highest cyclic CO₂ capacity. In addition to that, the cyclic capacity is still high for an evacuation at 0.2 bar. The increasing capacity at higher pressures also relates to a tripling in cyclic capacity for case c) compared to case a). Whereas it is not realistic to saturate the column completely with CO₂ during adsorption – this would lead to a breakthrough of all impurities and a contamination of the column – it is in principle possible to carry out the HP at higher pressures with the feed CO₂ partial pressure being the maximum reasonable pressure. This would require an additional compressor. In addition, more CO₂ is needed for a purge at higher pressures due to the higher CO₂ uptake. However, for Cu-TDPAT, it might still be favorable because of the drastic increase in cyclic capacity. The same holds true for AC, where the cyclic capacity for case c) is more than twice that of case a). For both zeolites, however, the increase in cyclic capacity when performing the heavy purge at higher pressures is less pronounced, because the CO₂ uptake at 1 bar is already close to its maximum, and performing the HP at higher pressures therefore does not seem very promising.

Because the CO₂ isotherm on Cu-TDPAT is not very steep, evacuation is sufficient for cleaning the column and case d) with a complete regeneration does not feature a significantly higher cyclic capacity than case a). This is similar for AC but very different for both zeolites: due to their high affinity for CO₂ and steep isotherm, the cyclic capacities between 1 bar and 0.1 bar (case a) or 0.2 bar (case b) are much lower than between 1 bar and complete regeneration. For case d), zeolite 13X outperforms all other materials. Therefore, a LP is essential for both zeolites to desorb additional CO₂ and thereby increase the cyclic capacity. For Cu-TDPAT and AC, the LP seems to be less critical.

Overall, based on this simple adsorption metric, in a cycle with a thorough regeneration, zeolite 13X is expected to perform very well whereas in a cycle with higher HP pressures, Cu-TDPAT features beneficial adsorbent metrics. For choosing the right boundaries for calculating the cyclic capacity, a good understanding of the process is necessary, which leads to accounting for the fact that the column can be regenerated deeper when adding a LP (case d) or that the HP could be carried out at higher pressures (case c), which results in different preferred adsorbents.

However, the CO₂ cyclic capacity is by far not enough to assess the process performance. As an example: whereas zeolite CaX looks more promising than zeolite 13X for case a)-c), the high heat of adsorption for CO₂ makes it less promising for actual application. In addition, it features a less favorable impurity adsorption profile, which makes it difficult to purify hydrogen. The effect of the impurities for purifying both CO₂ and H₂ will be addressed in the next section.

6.2 The role of impurity adsorption

For purifying H₂, not only CO₂ adsorption, but also adsorption of all impurities is important. The slower the impurity fronts propagate, the longer the duration of the adsorption step during which high purity H₂ can be produced. It is clear from Figure 26 that there is a significant difference in the uptake of impurities and of H₂. For most adsorbents, the adsorption strength increases from H₂ with a low affinity over Ar, N₂, CH₄ and CO and finally CO₂ with the strongest adsorption. This makes it clear that whereas N₂ and Ar (relevant for ATR) are likely to break through early and reduce the attainable H₂ purity, CH₄ and CO are more likely to contaminate the CO₂ product.

There are significant differences between the different materials. When comparing N₂ adsorption, the differences are particularly striking: N₂ uptake is very low on Cu-TDPAT and particularly high on zeolite CaX. For the feed partial pressure of 0.05 bar (compare Table 7), the N₂ uptake is reported in Table 19. Whereas it is similar on zeolite 13X and AC, the uptake on Cu-TDPAT is only half that and the uptake on zeolite CaX is more than three times higher than on zeolite 13X. The H₂ uptake at feed partial pressure (Table 19) is particularly low on zeolite 13X, slightly higher on Cu-TDPAT and even higher on AC. CH₄ has the highest uptake on Cu-TDPAT (at 1 bar), but the affinity is higher on the other materials, whereas CO adsorbs stronger than CH₄ on both Cu-TDPAT and zeolite CaX.

In Table 19, the uptake of the different gases on the different materials is shown at the feedstream partial pressure as reported in Table 7 and a temperature of 25 °C, assuming that there is no competition between the different adsorbates. Note that the feed partial pressure for CO is above 1 bar (1.16 bar) and the values reported in the table have been extrapolated.

Table 19 – Uptake of the different components on different materials at feedstream partial pressure and a temperature of 25 °C. Zero competition is assumed.

	<i>p</i> in bar	Zeolite 13X	Zeolite CaX	AC	Cu-TDPAT
H ₂	19	0.40	-	1.20	0.57
CO ₂	4	6.06	5.01	3.69	9.74
CO	1.16	-	1.09	-	1.14
CH ₄	0.76	0.59	0.47	0.58	0.74
N ₂	0.05	0.022	0.071	0.020	0.012

Dividing this uptake by the molar fraction of component *i* in the feed, y_i^{feed} , gives the amount of feed for which, in equilibrium with the column, all of component *i* would be adsorbed and the column would be completely saturated under the assumption that the uptake of the component is not reduced or enhanced by the other components in the feed. This gives an indication of the molar amount of feed that can be fed to a column per mass of adsorbent until the component breaks through. We call this here the characteristic feed loading for component *i*, c_i^{feed} .

$$c_i^{\text{feed}} = q_i^{\text{feed}} / y_i^{\text{feed}}$$

The higher this value, the longer until breakthrough. Even though this is a very simplified metric, it can reveal some interesting characteristics of the different adsorbent materials and is reported in

Table 20.

The characteristic feed loading is the lowest for H₂ and an order of magnitude lower than for all others. This means that the H₂ breaks through very quickly and can be produced as light product.

The next lowest characteristic feed loading is for the one of N_2 for all adsorbents except zeolite CaX. This means that N_2 is the first impurity to break through. For Cu-TDPAT, however, $c_{N_2}^{feed}$ is less than 8 times $c_{H_2}^{feed}$ due to the low N_2 adsorption. This means that the duration of the adsorption has to be stopped very early when all other impurities are still far from the column top and relates to a 'waste' of adsorbent material and the high uptake of the other gases, because the majority of the adsorbent is only used to (poorly) adsorb N_2 without being in contact with other impurities or CO_2 . For CO_2 , for example, 10 times more feed could be accepted for mass of adsorbent before it breaks through. This makes a co-production of CO_2 difficult, because high recycle ratios of CO_2 are needed to saturate the column in the HP. This translates to higher energy consumption or could make the separation unfeasible. For zeolite CaX, however, $c_{N_2}^{feed}$ is very high due to the strong N_2 adsorption. Therefore, mixing both adsorbents (Cu-TDPAT and zeolite CaX) may be promising for enhancing the N_2 adsorption, while still harvesting Cu-TDPAT's otherwise very promising adsorption characteristics.

Table 20 – Characteristic feed loading representing the uptake of component i at feed partial pressure divided by molar fraction in the feed assuming no competition. This is an indicator for the molar amount of feed a certain mass of adsorbent can be contacted with before the bulk of the component breaks through.

	unit	Zeolite 13X	Zeolite CaX	AC	Cu-TDPAT
$c_{H_2}^{feed}$	[mol _{Feed} /m _{ads}]	0.53	-	1.58	0.75
$c_{CO_2}^{feed}$	[mol _{Feed} /m _{ads}]	37.1	30.7	22.6	59.7
c_{CO}^{feed}	[mol _{Feed} /m _{ads}]	-	23.5	-	24.5
$c_{CH_4}^{feed}$	[mol _{Feed} /m _{ads}]	19.4	15.6	19.0	24.5
$c_{N_2}^{feed}$	[mol _{Feed} /m _{ads}]	10.9	35.3	10.1	5.9

Whereas a higher $c_{N_2}^{feed}$ is favorable for enhancing the H_2 purity and extending the feed duration, when the c_i^{feed} of an impurity is very close to that of CO_2 , this also shows that it might become problematic to separate the impurity from the CO_2 stream. This is for example the case for CH_4 on AC, as explained in D1.1.1 [3]. The same could happen for CO on zeolite CaX, where both c_i^{feed} are close to another. For $c_{N_2}^{feed}$, however, a high value is not problematic due to its low concentration in the feed: even if all the N_2 would end up in the CO_2 product, the required purity could still be reached.

Overall, whereas Cu-TDPAT shows promise for VPSA for co-production of CO_2 and H_2 , its weak N_2 adsorption seem to make it difficult to obtain H_2 at the required purities. Zeolite 13X on the other hand seems to be a favorable adsorbent when taking into consideration the uptake of the different impurities and the low H_2 adsorption, even though it features a lower cyclic capacity than Cu-TDPAT, unless the column is regenerated deeply. Whereas zeolite CaX looks more promising than zeolite CaX in terms of the cyclic CO_2 capacity and the stronger N_2 adsorption, an increasing contamination of the CO_2 product with CO might become an issue. In addition, it features a very high heat of adsorption as

discussed in section 4.3.1, which is unfavorable for the separation. A mixing of Cu-TDPAT with zeolite CaX could solve the issue of the first's low N₂ adsorption. AC shows less promise for the separation than the other materials because of a low CO₂ cyclic capacity and a strong CH₄ adsorption, which makes it difficult to obtain CO₂ at the required purity with a high recovery.

7 MIXED-MATRIX ADSORBENTS

Nitrogen adsorption on Cu-TDPAT is lower than on zeolite 13X and significantly lower than on zeolite CaX. However, in VPSA processes that target a typical SMR+WGS syngas as reported in Table 7, nitrogen is the leading impurity front for AC, Cu-TDPAT and zeolite 13X and therefore key for reaching high H₂ purities. Therefore, a high nitrogen adsorption is favorable and can become critical for reaching the required separation performance. Especially for high adsorption strengths of all other impurities and CO₂, increasing the N₂ adsorption is important to be able to extend the duration of the adsorption step. Otherwise, the strong adsorption capacity for the other adsorbates is wasted. Mixing Cu-TDPAT with zeolite CaX could be an option to increase the N₂ adsorption. Mixtures at different mixing ratios have been examined with 40 w% Cu-TDPAT, 60 w% Cu-TDPAT and 80 w% Cu-TDPAT and characterized in terms of adsorption isotherms and heats of adsorption.

7.1 Adsorption isotherms

The measured adsorption isotherms of CO₂, CH₄, CO and N₂ on the three different mixtures of zeolite CaX and Cu-TDPAT are shown in Figure 27 together with the fitted DSL isotherms for three different temperatures. The corresponding isotherm parameters are reported in Table 21 for the mixture with 60 w% CaX, in Table 22 for the mixture with 40 w% CaX and in Table 23 for the mixture with 20 w% CaX.

It is clear from Figure 27 that an addition of more zeolite CaX to Cu-TDPAT decreases the adsorbed amount of CO₂ but increases the steepness of the CO₂ isotherm (left side compared to right side). This is expected from the single adsorbent isotherms for Cu-TDPAT and zeolite CaX, as shown before. For both CH₄ and CO, the trend is the same as for CO₂ (decreasing adsorbed amount but increasing steepness of the isotherm for increasing the CaX content). For N₂, however, both the adsorbed amount and the steepness of the isotherm increase significantly when adding zeolite CaX to Cu-TDPAT. E.g. for 1 bar, the nitrogen adsorption of a 40 w% Cu-TDPAT mixture is approximately 50 % higher than that of an 80 w% Cu-TDPAT mixture. Therefore, the approach of mixing adsorbents seems promising for achieving the adsorption characteristics required.

However, it also comes with limitations, such as reducing the maximum temperature that can be used for regenerating zeolite CaX to 220 °C in order to avoid decomposition of the MOF. In practice, either using pellets that contain both adsorbent materials in the desired ratio, or mixing particles of one and of the other adsorbent, are possible. The latter is more flexible and could be favorable especially when the best mixing ratio has not been established yet, but could result in unwanted segregation. Using layered beds with Cu-TDPAT and CaX is another option to combine both materials. Whereas zeolite CaX is a promising material in this context due to its strong N₂ adsorption, also mixing Cu-TDPAT with other materials could be promising, for example with zeolite 13X, which features a higher N₂ adsorption than Cu-TDPAT but also very favorable adsorption characteristics for CO₂.

For process modelling, we recommend to use the Sips isotherms fitted for adsorption on pure Cu-TDPAT and pure zeolite CaX (as provided in the previous sections) weighted by their respective mass fraction.

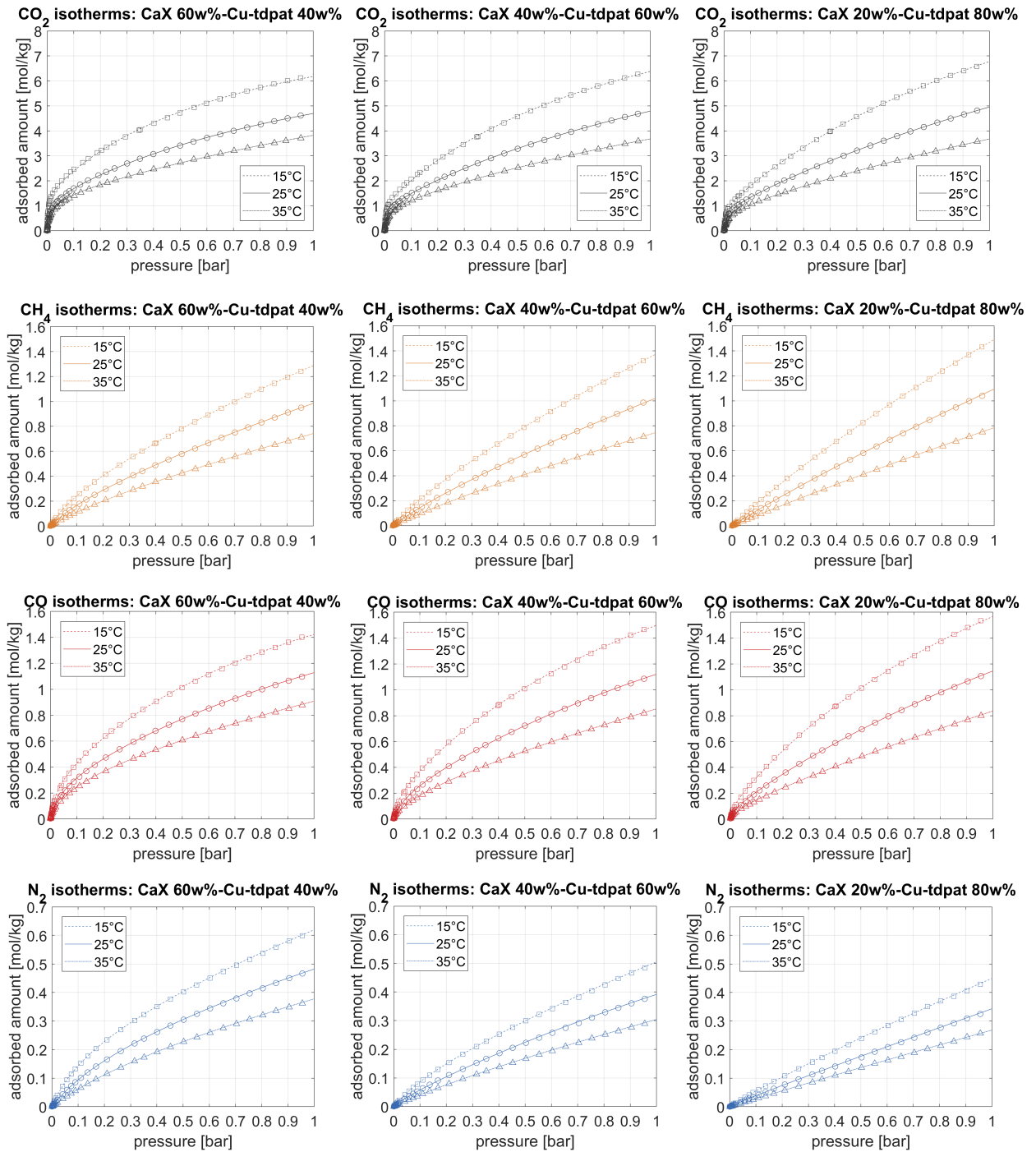


Figure 27 – Measured isotherms on zeolite CaX-Cu-TDPAT mixtures at 15 °C (squares), 25 °C (circles) and 35 °C (triangles) for different gases (CO₂, CH₄, CO and N₂). Three mixtures with 40, 60 and 80 w% Cu-TDPAT were measured and are shown from left to right. The fitted DSL isotherms for the different temperatures are shown as lines with the isotherm parameters reported in Table 21, Table 22 and Table 23 for 40, 60 and 80 w% Cu-TDPAT, respectively.

Table 21 – DSL parameters for CO₂, CH₄, CO and N₂ on a mixture of 40 w% Cu-TDPAT and 60 w% zeolite CaX for 15, 25 and 35 °C.

	unit	<i>T</i>	CH ₄	CO	CO ₂	N ₂
a_i^{inf}	[mol/kg]	288	0.20573	0.28291	1.4450	0.20816
b_i	[1/ bar]	288	11.281	44.239	403.05	7.9270
c_i^{inf}	[mol/kg]	288	5.6497	2.4444	8.2452	2.6209
d_i	[1/ bar]	288	0.24138	0.88402	1.3525	0.19887
a_i^{inf}	[mol/kg]	298	0.17438	0.28000	1.2200	0.17903
b_i	[1/ bar]	298	6.8100	22.754	104.22	4.4040
c_i^{inf}	[mol/kg]	298	6.1452	2.6517	8.0420	2.1893
d_i	[1/ bar]	298	0.15675	0.48029	0.76600	0.18159
a_i^{inf}	[mol/kg]	308	0.16055	0.28000	1.3400	0.17957
b_i	[1/ bar]	308	3.7264	14.997	50.175	2.41025
c_i^{inf}	[mol/kg]	308	7.6175	3.1736	10.418	4.00916
d_i	[1/ bar]	308	0.087999	0.25552	0.31716	0.066733

Table 22 – DSL parameters for CO₂, CH₄, CO and N₂ on a mixture of 60 w% Cu-TDPAT and 40 w% zeolite CaX for 15, 25 and 35 °C.

	unit	<i>T</i>	CH ₄	CO	CO ₂	N ₂
a_i^{inf}	[mol/kg]	288	0.12023	0.18097	1.08	0.10275
b_i	[1/ bar]	288	8.6471	60.269	423.00	6.2485
c_i^{inf}	[mol/kg]	288	7.4179	3.0745	10.766	3.6193
d_i	[1/ bar]	288	0.20552	0.75208	0.97196	0.13022
a_i^{inf}	[mol/kg]	298	0.13001	0.18	1.01330	0.02
b_i	[1/ bar]	298	4.5013	24.526	118.11	17.684
c_i^{inf}	[mol/kg]	298	9.4404	3.2015	10.818	1.9300

d_i	[1/ bar]	298	0.10719	0.41988	0.53887	0.23953
a_i^{inf}	[mol/kg]	308	0.11734	0.18	1	0.045977
b_i	[1/ bar]	308	2.4164	13.801	55.722	3.5688
c_i^{inf}	[mol/kg]	308	8.9606	4.7676	10	3.9866
d_i	[1/ bar]	308	0.079831	0.16739	0.36938	0.072224

Table 23 – DSL parameters for CO₂, CH₄, CO and N₂ on a mixture of 80 w% Cu-TDPAT and 20 w% zeolite CaX for 15, 25 and 35 °C.

	unit	T	CH ₄	CO	CO ₂	N ₂
a_i^{inf}	[mol/kg]	288	0.039931	0.098285	0.92098	0.011342
b_i	[1/ bar]	288	7.57068	125.39	294.72	14.087
c_i^{inf}	[mol/kg]	288	8.42377	3.6125	14.788	4.4903
d_i	[1/ bar]	288	0.20895	0.68586	0.65620	0.10840
a_i^{inf}	[mol/kg]	298	0.041793	0.09	0.87817	0.011112
b_i	[1/ bar]	298	4.1631	44.419	105.25	7.9483
c_i^{inf}	[mol/kg]	298	11.384	4.0359	15.591	26.191
d_i	[1/ bar]	298	0.10281	0.35500	0.35536	0.012892
a_i^{inf}	[mol/kg]	308	0.025109	0.09	0.82363	0.011970
b_i	[1/ bar]	308	2.2815	24.769	51.864	0.079536
c_i^{inf}	[mol/kg]	308	10.796	5.8554	13.884	6.6700
d_i	[1/ bar]	308	0.076552	0.14675	0.26029	0.041788

7.2 Isosteric heat of adsorption

The heats of adsorption averaged over all three temperatures are shown in Figure 28 for the three different mixed-matrix adsorbents. With a higher Cu-TDPAT content, the isosteric heat of adsorption for CO₂, N₂ and CH₄ decreases whereas it increases CO. This is consistent with the isosteric heats determined for the single adsorbents. It is important to note that even for an addition of only 20 w% zeolite CaX, the isosteric heat of adsorption is very high for CO₂, which could make the separation more difficult.

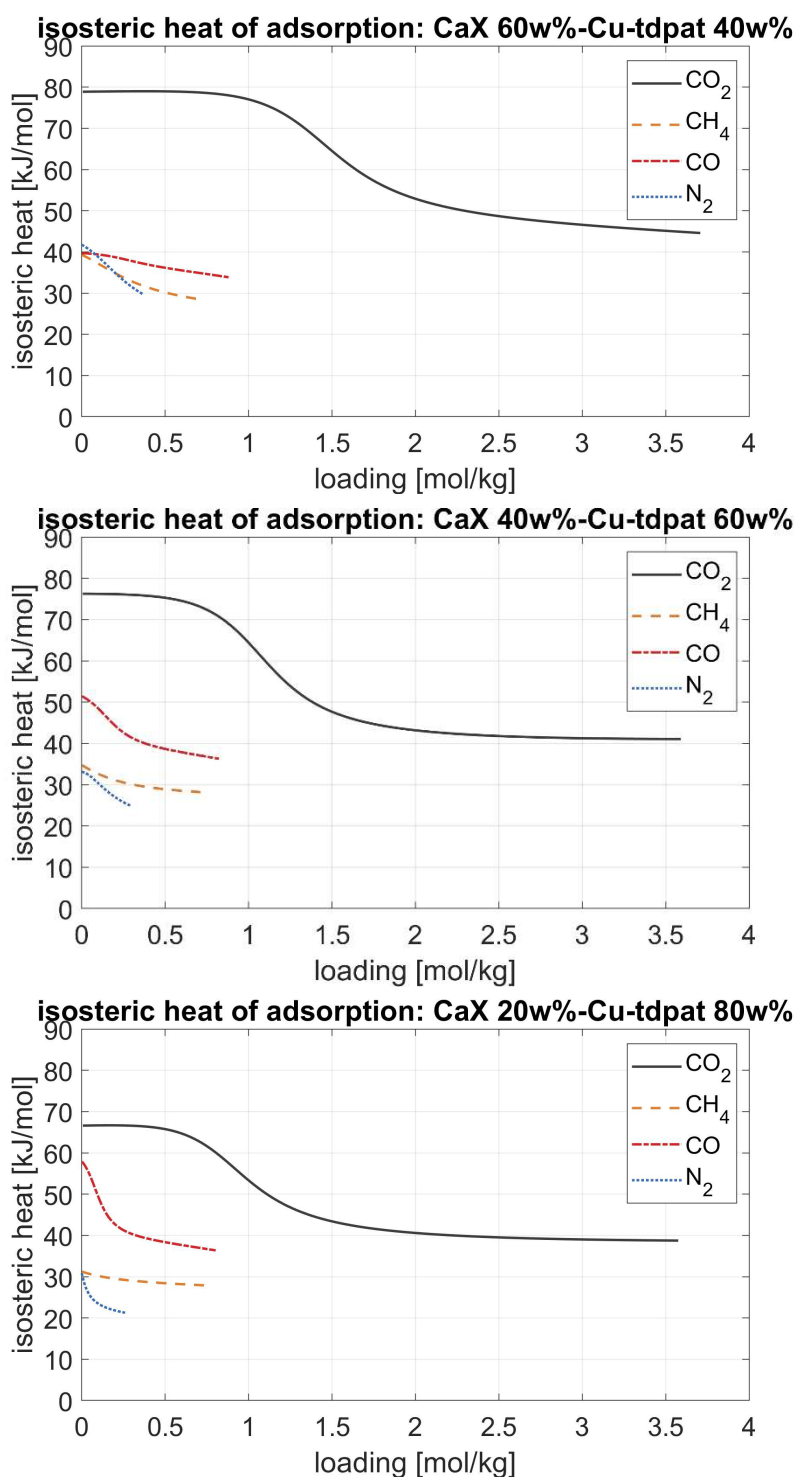


Figure 28 – Isosteric heat of adsorption for CO₂, CH₄, CO and N₂ on zeolite CaX-Cu-TDPAT mixtures for different loadings averaged over temperature (15, 25 and 35 °C). Only the loadings up to which measurements for all three temperatures were available were considered for the evaluation.

8 SUMMARY AND CONCLUSION

In this report, the characterization of various commercial and novel adsorbents and mixtures thereof, which are promising for H₂-CO₂-impurity separation using vacuum pressure swing adsorption (VPSA), are summarized.

As first step, a sensitivity analysis was carried out to show the influence of material related parameters like the adsorption isotherms, the heats of adsorption and the mass transfer coefficients on the separation performance. It was found that the influence of both the CO₂ mass transfer coefficient and the heat of adsorption for CO₂ are high and result in missing the target separation specifications of 99.97 % H₂ purity, 96 % CO₂ purity and a minimum of 90 % recovery for both. When varying the heats of adsorption and mass transfer coefficients of all the impurities (CO, CH₄, N₂), however, the separation target could still be reached with the change in performance indicators being below 1 % (0.01 % for H₂ purity). The mass transfer coefficient and heat of adsorption of H₂ affected the KPIs even less. Changing the adsorption isotherms by eliminating the temperature dependence or varying the maximum capacity for a specific component resulted in larger variations and the separation target could not be reached, except for varying H₂ adsorption. Even completely neglecting H₂ adsorption still resulted in reaching all separation requirements except for the H₂ recovery, which is still above 89 %. From this analysis it can be concluded that whereas an estimation of the heat of adsorption and mass transfer is critical for CO₂, an accurate description of the adsorption isotherms including the temperature dependency is essential for CO₂ and all impurities. The H₂ isotherm, however, plays a less important role due to its low adsorption.

Subsequently, promising commercial adsorbents were characterized starting with zeolite 13X. Because zeolite 13X performs particularly well for VPSA, in addition to measuring adsorption isotherms, also binary and ternary breakthrough experiments with CO₂-CH₄-H₂ mixtures were performed. Mass and heat transfer coefficients were estimated based on these experiments making use of the same column model as used for the sensitivity analysis. The model could reproduce the experimental results very well for binary breakthrough experiments. Overall, the breakthrough was governed by the rate of heat transfer rather than the rate of mass transfer and constant mass transfer coefficients could be used to fit all experiments. In contrast to that, the internal heat transfer coefficient was found to have a stronger influence on the breakthrough temperature and composition profiles and should be fit to each experiment individually. It was in the range of 20-40 W/m²K for the performed experiments. The agreement between the ternary breakthrough experiments and the simulation was worse, but also here the constant mass transfer coefficients worked well. Mass transfer of H₂ on zeolite 13X was found to be fast with a linear driving force coefficient of $k_{\text{H}_2} = 1 \text{ s}^{-1}$. Mass transfer of CH₄ is slower with $k_{\text{CH}_4} = 0.5 \text{ s}^{-1}$ and slowest for CO₂ with $k_{\text{CO}_2} = 0.1 \text{ s}^{-1}$.

In addition to zeolite 13X, isotherms were measured on two other commercial materials, namely zeolite CaX and AC AP3-60. Both zeolites and AC are readily available at large quantities and low cost, and therefore very promising for an application that is time critical, targeting a large scale and has to be cost-competitive. In addition to the commercial adsorbents, a novel metal organic framework, namely Cu-TDPAT, and mixtures of Cu-TDPAT and zeolite CaX were examined.

For all those materials, temperature dependent isotherms of CO₂, several of the impurities commonly present in H₂ production processes (CH₄, N₂, CO, Ar), and H₂ (except for CaX and CaX-mixtures) were measured. All isotherms were fitted to a temperature dependent Sips isotherm equation and the heats of adsorption were computed. For all adsorbents, CO₂ adsorbs the strongest and H₂ the weakest with the CO₂ isotherm being very steep for both zeolites and much flatter for Cu-TDPAT and AC. For Cu-TDPAT, however, the uptake of CO₂ is very high with a maximum capacity around 20 mol/kg, which is approximately four times that of the zeolites and more than twice that of AC. This high uptake can potentially compensate for the lower affinity and in addition makes it easier to regenerate the adsorbent.

The CO₂ cyclic capacity was computed for all pure adsorbents and it was shown that it is essential to choose partial pressures for CO₂ adsorption and desorption that are representative of the cycle. Whereas CO₂ adsorbs at around 4 bar partial pressure, the column is not saturated with CO₂ at this pressure, but the adsorption step stops before the first impurity reaches the column top to prevent contaminating the H₂ product. The column is saturated with CO₂ during a subsequent HP step, which is carried out at ambient pressure for zeolite 13X, but could also be carried out at higher pressure. This increases the cyclic capacity for Cu-TDPAT and AC significantly, but requires an additional compressor and energy. For desorption, the column is evacuated and purged. Whereas the purge is not essential for Cu-TDPAT and AC as their lower CO₂ affinity makes them easier to regenerate with evacuation only, it is crucial for both zeolites, which feature a very strong CO₂ adsorption even at 0.1 bar. A complete regeneration more than doubles their cyclic capacity compared to evacuation only. Overall, Cu-TDPAT is the most promising adsorbent for higher HP pressures and incomplete regeneration, whereas zeolite 13X is the most promising adsorbent when the HP is carried out at ambient pressure and close to complete regeneration can be achieved during the light purge.

In addition to the CO₂ cyclic capacity, also the uptake of the impurities plays an important role for purifying both H₂ and CO₂. The impurities typically increase in adsorption strength starting from Ar, over N₂, to CH₄ and CO with a similar adsorption strength. This leads to Ar and N₂ breaking through early and therefore being critical for reaching a high H₂ purity, and to CO and CH₄ breaking through later with propagation velocities close to CO₂, thereby potentially contaminating the CO₂ product.

For AC, CH₄ adsorption had previously been found to be so strong that it limits the attainable CO₂ purity [3]. Something very similar could happen for CO on zeolite CaX due to a strong CO adsorption. For zeolite 13X and Cu-TDPAT, the uptake of both CO (based on literature values for zeolite 13X) and CH₄ seems to be sufficiently low to guarantee the production of high purity CO₂.

N₂ adsorption, however, is very low on Cu-TDPAT, which translates to an early N₂ breakthrough in a VPSA process for H₂-CO₂-impurity separation and therefore makes the purification of H₂ difficult. To be able to exploit the otherwise very favorable adsorption characteristics, including also a low heat of adsorption for CO₂ in the range of 30 kJ/mol, a mixing with zeolite CaX was assessed. CaX features a particularly strong N₂ adsorption: in contrast to the other adsorbents, the affinity towards N₂ is higher than towards CH₄ and the uptake at feed partial pressure around twice that of zeolite 13X and AC.

Measuring the adsorption isotherms of three discrete mixtures of Cu-TDPAT and zeolite CaX with 20, 40 and 60 w% CaX did reveal that the N₂ uptake of Cu-TDPAT can be increased significantly by an addition of as little as 20 w% zeolite CaX, which could lead to process improvements. However, the CO₂ cyclic capacity and uptake decreases significantly and the heat of adsorption for CO₂ increases when adding zeolite CaX, which are both unfavorable for a VPSA process.

To sum up, zeolite 13X naturally features favorable adsorption characteristics for all impurities and CO₂ and is promising for cycles with a HP at ambient pressure and a thorough regeneration during a light purge. In contrast to that, Cu-TDPAT features some beneficial characteristics like a low heat of adsorption for CO₂ and a high CO₂ cyclic capacity, especially for a HP at above ambient pressure, together with a high uptake of both CO and CH₄. The limited N₂ uptake, however, might limit its usability for producing high H₂ purities. Mixing it with another adsorbent like zeolite CaX enhances the N₂ adsorption and thereby potentially the performance, but also leads to a lower CO₂ cyclic capacity and a higher heat of adsorption. Both AC and zeolite CaX seem less promising for the VPSA, in particular for reaching high CO₂ purities.

Overall, commercial adsorbents still have a large potential for H₂-CO₂-impurity separation, but also novel MOFs or a combination of both could be interesting. It is essential to thoroughly understand the adsorption process to determine which adsorbent has the most potential or how the process can be adapted to be more suitable for another adsorbent. Only by combining material and process in the best possible way, the performance of a VPSA process can be optimized. With this thorough characterization of different commercial and novel materials, a good starting point for simultaneous material and process optimization is available to pave the way towards truly efficient adsorption based CO₂-H₂-impurity separation. Such an efficient separation process could act as key technology for coupling fossil fuel based H₂ production with carbon capture and storage (CCS) with uses for industry, transportation and heating and thereby be an important enabler for a low carbon economy through H₂ and CCS.

BIBLIOGRAPHY

- [1] M. Voldsund, K. Jordal y R. Anantharaman, «Hydrogen production with CO₂ capture,» *Int. J. Hydrogen Energy*, vol. 41, nº 9, p. 4969–4992, 2016.
- [2] IEAGHG, «International Energy Agency (IEA), “Techno - Economic Evaluation of SMR Based Standalone (Merchant) Hydrogen Plant with CCS,» 2017.
- [3] A. Streb, M. van der Spek, M. Gazzani, D. Sutter, C. Antonini y M. Mazzotti, «D1.1.1: Report on new PSA and VPSA cycles for sharp separation of CO₂, H₂ and impurities,» 2018.
- [4] A. Streb, M. Hefti, M. Gazzani y M. Mazzotti, «A novel adsorption process for co-production of hydrogen and CO₂ from a multicomponent stream,» *Ind. Eng. Chem. Res.*, 2019.
- [5] J. Schell, N. Casas, R. Pini y M. Mazzotti, «Pure and binary adsorption of CO₂, H₂ and N₂ on activated carbon,» *Adsorption*, vol. 18, nº 1, pp. 49-65, 2012.
- [6] S. Ottiger, R. Pini, G. Storti y M. Mazzotti, «Competitive adsorption equilibria of CO₂ and CH₄ on dry coal,» *Adsorption*, vol. 14, p. 539–556, 2008.
- [7] R. Pini, S. Ottiger, A. Rajendran, G. Storti y M. Mazzotti, «Reliable measurement of near-critical adsorption by gravimetric method,» *Adsorption*, vol. 12, nº 5, p. 393–403, 2006.
- [8] M. Asgari, R. Semino, P. Schouwink, I. Kochetygov, O. Trukhina, J. D. Tarver, S. Bulut, S. Yang, C. M. Brown y M. C. W. L. Queen, «An In-Situ Neutron Diffraction and DFT Study of Hydrogen Adsorption in a Sodalite-Type Metal–Organic Framework, Cu-BTtri,» *Eur. J. Inorg. Chem.*, p. 1147–1154, 2019.
- [9] H. S. Sherry, «The Ion-Exchange Properties of Zeolites. IV. Alkaline Earth Ion Exchange in the Synthetic Zeolites Linde X and Y,» *J. Phys. Chem.*, pp. 4086-4094, 1968.
- [10] B. Li, Z. Zhang, Y. Li, K. Yao, Y. Zhu, Z. Deng, F. Yang, X. Zhou, G. Li, H. Wu, N. Nijem, Y. J. Chabal, Z. Lai, Y. Han, Z. Shi, S. Feng y J. Li, «Enhanced Binding Affinity, Remarkable Selectivity, and High Capacity of CO₂ by Dual Functionalization of a rht-Type Metal–Organic Framework,» *Angew. Chem. Int. Ed.*, p. 1412 –1415, 2012.
- [11] A. Streb, M. van der Spek, M. Gazzani, D. Sutter, C. Antonine y M. Mazzotti, «M1.1.2: Design of the experimental rig for VPSA cycles completed,» 2018.

- [12] D. Marx, L. Joss, M. Hefti y M. Mazzotti, «Temperature Swing Adsorption for Postcombustion CO₂ Capture: Single- and Multicolumn Experiments and Simulations,» *Ind. Eng. Chem. Res.*, vol. 55, nº 5, p. 1401–1412, 2016.
- [13] N. Casas, J. Schell, R. Pini y M. Mazzotti, «Fixed bed adsorption of CO₂/H₂ mixtures on activated carbon: experiments and modeling,» *Adsorption*, vol. 18, nº 2, pp. 143-161, 2012.
- [14] Y. K. Ryu, S. J. Lee, J. W. Kim y C.-H. Lee, «Adsorption equilibrium and kinetics of H₂O on zeolite 13x,» *Korean J. Chem. Eng.*, p. 525–530, 2001.
- [15] J. G. Jee, J. S. Lee y C. H. Lee, «Air separation by a small-scale two-bed medical O₂ pressure swing adsorption,» *Ind. Eng. Chem. Res.*, pp. 3647-3658, 2001.
- [16] Y. Park, Y. Ju, D. Park y C. H. Lee, «Adsorption equilibria and kinetics of six pure gases on pelletized zeolite 13X up to 1.0 MPa: CO₂, CO, N₂, CH₄, Ar and H₂,» *Chem. Eng. J.*, vol. 292, p. 348–365, 2016.
- [17] V. S. Balashankar, A. K. Rajagopalan, R. d. Pauw, A. M. Avila y A. Rajendran, «Analysis of a Batch Adsorber Analogue for Rapid Screening of Adsorbents for Postcombustion CO₂ Capture,» *Ind. Eng. Chem. Res.*, pp. 3314-3328, 2019.
- [18] S. Sircar y T. C. Golden, «Purification of Hydrogen by Pressure Swing Adsorption,» *Sep. Sci. Technol.*, vol. 35, nº 5, p. 667–687, 2000.
- [19] M. Hefti, D. Marx, L. Joss y M. Mazzotti, «Adsorption equilibrium of binary mixtures of carbon dioxide and nitrogen on zeolites ZSM-5 and 13X,» *Microporous Mesoporous Mat.*, pp. 215-228, 2015.
- [20] J. A. Ritter, S. J. Bhadra y A. D. Ebner, «On the Use of the Dual-Process Langmuir Model for Correlating Unary Equilibria and Predicting Mixed-Gas Adsorption Equilibria,» *Langmuir*, p. 4700–4712, 2011.
- [21] S. García, J. J. Pis, F. Rubiera y C. Pevida, «Predicting Mixed-Gas Adsorption Equilibria on Activated Carbon for Precombustion CO₂ Capture,» *Langmuir*, pp. 6042-6052, 2013.
- [22] J. G. Jee, M. B. Kim y C. H. Lee, «Adsorption characteristics of hydrogen mixtures in a layered bed: Binary, ternary, and five-component mixtures,» *Ind. Eng. Chem. Res.*, vol. 40, nº 3, p. 868–878, 2001.
- [23] M. Hefti, L. Joss, D. Marx y M. Mazzotti, «An Experimental and Modeling Study of the Adsorption Equilibrium and Dynamics of Water Vapor on Activated Carbon,» *Ind. Eng. Chem. Res.*, vol. 54, pp. 12165-12176, 2015.

- [24] J. Li, X. Wang, G. Zhao, C. Chen, Z. Chai, A. Alsaedi, T. Hayat y X. Wang, «Metalorganic framework-based materials: Superior adsorbents for the capture of toxic and radioactive metal ions,» *Chemical Society Reviews*, p. 2322–2356, 2018.
- [25] R. K. Motkuri, C. A. F. J. Liu, S. K. Nune, P. Thallapally y B. P. McGrail, «Metal organic frameworks—synthesis and applications,» de *Industrial Catalysis and Separations: Innovations for Process Intensification*, CRC Press, 2014, p. 63–78.
- [26] H. Li, K. Wang, Y. Sun, C. T. Lollar, J. Li y H. C. Zhou, «Recent advances in gas storage and separation using metal–organic frameworks,» *Materials Today*, p. 108–121, 2018.
- [27] Z. Hu, Y. Wang, B. B. Shah y D. Zhao, «CO₂ Capture in Metal-Organic Framework Adsorbents: An Engineering Perspective,» *Adv. Sustainable Syst.*, p. 1800080, 2019.
- [28] A. K. Rajagopalan y A. Rajendran, «The effect of nitrogen adsorption on vacuum swing adsorption based post-combustion CO₂ capture,» *International Journal of Greenhouse Gas Control*, vol. 78, pp. 437-447, 2018.
- [29] V. I. Agueda, J. A. Delgado, M. A. Uguina, P. B. Aud, I. Spjelkavik, R. Blom y C. Grande, «Adsorption and diffusion of H₂, N₂, CO, CH₄ and CO₂ in UTSA-16 metal-organic framework extrudates,» *Chem. Eng. Sci.*, 159-169 2015.
- [30] N. Al-Janabi, P. Hill, L. Torrente-Murciano, A. Garforth, P. Gorgojo, F. Siperstein y X. Fan, «Mapping the Cu-BTC metal–organic framework (HKUST-1) stability envelope in the presence of water vapour for CO₂ adsorption from flue gases,» *Chem. Eng. J.*, vol. 281, pp. 669-677, 2015.
- [31] K. Zhang, A. Nalaparaju y J. Jiang, «CO₂ capture in rht metal–organic frameworks: multiscale modeling from molecular simulation to breakthrough prediction,» *J. Mater. Chem. A*, p. 16327–16336, 2015.
- [32] H. Wu, K. Yao, Y. Zhu, B. Li, Z. Shi, R. Krishna y J. Li, «Cu-TDPAT, an rht-Type Dual-Functional Metal–Organic Framework Offering Significant Potential for Use in H₂ and Natural Gas Purification Processes Operating at High Pressures,» *J. Phys. Chem.*, pp. 16609-16618, 2012.